Fall 2015

New Engineering Approaches to Arrhythmias and Myocardial Infarction

Frency Varghese
Old Dominion University, frency.varghese@gmail.com

NEW ENGINEERING APPROACHES TO ARRHYTHMIAS AND MYOCARDIAL INFARCTION

by

Frency Varghese
M.S. December 2009, Syracuse University
B.S. (Tech.) July 2004, University of Mumbai
B.S. May 2000, University of Mumbai

A Dissertation Submitted to the Faculty of
Old Dominion University in Partial Fulfillment of the
Requirements for the Degree of

DOCTOR OF PHILOSOPHY

BIOMEDICAL ENGINEERING

OLD DOMINION UNIVERSITY
December 2015

Approved by:

_____
Christian Zemlin (Director)

_____
Barbara Hargrave (Member)

_____
Michel Audette (Member)

_____
Dean Krusienski (Member)

_____
Andrei Pakhomov (Member)

ABSTRACT

NEW ENGINEERING APPROACHES TO ARRHYTHMIAS AND MYOCARDIAL INFARCTION

Frency Varghese
Old Dominion University, 2015
Director: Christian Zemlin

In this thesis, we present new engineering approaches to several important cardiac diseases. Chapter 1 considers the dynamics of arrhythmias. The most dangerous arrhythmias are reentrant arrhythmias, including ventricular fibrillation and ventricular tachycardia. During these arrhythmias, there are one or several rotating excitation waves present in the heart. Because of their shape, these waves are called scroll waves; their center of rotation is a one-dimensional curve called the filament. Filaments largely constrain the configuration of a scroll wave but are much simpler, so much effort has gone into describing scroll wave dynamics in terms of the dynamics of their filaments. In particular, the "geodesic principle" for filaments, which says that stable filaments are geodesics in a metric derived from the diffusivity, has been proposed and established for certain restrictive conditions. In this project, we show that the geodesic principle applies much more broadly, including for very large filament curvatures. We also discuss under which conditions the geodesic principle fails, particularly the case that the filament gets close to very heterogeneous substrate.

Chapters 2-4 introduce a new approach to cardiac defibrillation. The only existing effective treatment to ventricular fibrillation is to deliver high-energy electric shocks to

the heart using a defibrillator to terminate fibrillation and restore organized rhythm. Defibrillators currently available are effective in treating ventricular fibrillation, however, because of the large amount of energy deposited during the treatment can cause damaging effects to the tissue. In this project, we present results of a new technology using nanosecond pulsed electric fields to defibrillate the heart, while depositing only a fraction of energy needed by conventional defibrillators.

In the final part of this thesis, Chapters 5-7, we present results of an injectable therapeutic agent to regenerate the myocardium (heart muscle) affected by infarction. Myocardial infarction is a serious coronary artery disease that occurs when a coronary artery is so severely blocked that there is a dramatic reduction or complete disruption of blood supply, causing damage or death to the territory of the myocardium that was supplied by the blocked coronary vessel. Our results show how the injection of the therapeutic agent helps in preserving the electrical activity in the affected area, and also reduces pathological effects on the ejection fraction and heart rate.

In summary, we contribute to the understanding of the mechanisms of reentrant arrhythmias, develop new technology for ventricular defibrillation, and test a therapeutic agent for myocardial infarction.

I dedicate this thesis:

To my wife, Kavitha and son, Nathan: words are just not enough.

To my parents: taught me the importance of education.

To my brother, sister, and nieces - Susannah and Sarah.

ACKNOWLEDGMENTS

I would like to take this opportunity to express my gratitude to all those who have contributed to the successful completion of this dissertation.

Firstly, this dissertation would not have been possible without the guidance and mentorship of my advisor, Dr. Christian Zemlin. My association with Dr. Zemlin started while I was a graduate student at Syracuse University. Dr. Zemlin was my research advisor for my M.S. thesis, too. One characteristic of Dr. Zemlin that I have observed through the last many years is his patience and willingness to help. Once in Syracuse, while I was trying to meet thesis deadline, Dr. Zemlin sat through late night helping me edit and compile the thesis. Over the years, I have learned many things but one that stands out is his counsel of not to do quick fixes, especially while writing computer programs. I also try to be more patient and understanding in personal life. Once again, I would like to thank Dr. Zemlin for giving me an opportunity to work under him for my PhD and I consider it as my privilege.

I would also like to thank Dr. Michel Audette, Dr. Barbara Hargrave, Dr. Dean Krusienski and Dr. Andrei Pakhomov for accepting to be part of my dissertation committee. Their suggestions and remarks helped me navigate through the difficulties and bring this thesis to fruition.

I would like to express my gratitude to my many friends in Norfolk, Ms Kim McDonald, Dr. Kurnia and family, Morgans', Hardisons', Kings' Evers' Gibu and family, Pr. Gopal and Daisy, Dr. Earl Godfrey and family, Dr. Mark and Sarah Fernandes, who helped my wife and son stay busy while I was away in lab for long hours. I would also like to thank Hareen Shekhar, former ODU EE graduate student, who made sure that I had a place to stay when I first arrived at Norfolk. A special mention of my classmate and good friend, Finny Johnson from undergraduate days, and his family is also necessary.

I would like to thank my former and current colleagues Dr. Fei Xie, Sharath Sridhar, Joshua Lund, Alex Tichy, Mostafa Awwad, Anton Rekun, Tanvi Patel, and Johanna Neuber from our Cardiac Electrophysiology lab who at different time periods helped setup the lab and also with my experiments.

Finally and most importantly, this PhD would have been impossible without the support of my wife, Kavitha who sacrificed many of her dreams so that I could pursue mine. She was and is the pillar of support for me and my son, Nathan, and always encouraged and prayed for our success. I would also like to thank my family in India, my mom, brother, sister-in-law, sisters, brother-in-law, nieces, nephews, and my in-laws, who continually supported us while away from home.

However, all this would have remained a dream without the grace of God and prayers of many that I mentioned and those whom I missed out in this acknowledgement.

NOMENCLATURE

u	Activator
v	Inhibitor
ε	Permittivity
b	Outside Diameter of Pipe, inches
a	Modulus of Elasticity, lb/in2
D	Diffusion Tensor
d	diffusion coefficients
g	Metric Tensor
VF	Ventricular Fibrillation
SA	Sino Atrial
AV	Atrioventricular
ECG	Electrocardiogram
NsPEF	Nanosecond Pulsed Electric Field
R_{charge}	Charging Resistor
V_{BD}	Breakdown Voltage
C	Velocity of Light in Vacuum
ε_r	Relative Permittivity
TTC	Triphenyl Tetrazolium chloride
APD	Action Potential Duration
TA	Therapeutic Agent

TABLE OF CONTENTS

LIST OF TABLES

LIST OF FIGURES

DYNAMICS OF ARRHYTHMIAS

CHAPTER 1

INTRODUCTION: DYNAMICS OF ARRHYTHMIAS

The basic properties of cardiac tissue that permits impulse propagation are that cells have a stable resting state and that excitation can be induced with a sufficiently strong stimulus; this excitation can then propagate to resting neighboring cells. This property is called “excitability”, and it is shared by many other media besides the heart; they are called “excitable media”.

Phenomena such as the amoeba aggregation[1], transmission of impulses between neurons[2], and cardiac arrhythmias[3], can all be understood using the framework of excitable media[4]. An excitable medium is a continuous set of locally excitable entities like cardiac cells that can be stimulated independently[5]. These entities exhibit a threshold below which the media remains undisturbed in a stable state while any stimulation greater than the threshold will induce local transformation within the media[5].

Three-dimensional excitable media can maintain organized activity in the form of rotating, scroll-shaped waves. Scroll waves have been observed in a wide range of excitable media[6]–[10], most notably in the heart, where they cause life-threatening arrhythmias[11]–[13]. They are organized around vortex-like cores, called filaments, that can change shape or break up into multiple interacting fragments[14]–[16]. Filaments

can also become anchored (pinned), giving rise to stationary rotating scroll waves[17]–[19] which in the heart are linked to sustained arrhythmias.

Excitable media are governed by reaction-diffusion equations. The diffusion coefficient is one of the key parameters, defining the propagation velocity of the excitation wave[20]. In models of the heart, diffusion is described by a tensor, which represents the anisotropic electrical conductance of muscle fibers constituting the myocardial wall[21].

Here we focus of on the shape and the dynamics of anchored filaments in media with a discontinuous change in diffusion. In the heart, such discontinuities correspond to abrupt changes in fiber direction, which are characteristic of the outflow tract[22] and other regions of the myocardium[23]. These regions are linked to arrhythmias[24], but their mechanism remains largely unknown, which makes the investigation of the filament properties in media with discontinuities in diffusion particularly important.

We show that a discontinuity in diffusion makes the filament abruptly change its angle to the interface, reminiscent of the refraction of a light beam at the boundary separating domains with different optical density. There is also a critical angle of the filament to the interface, which cannot be exceeded. Using a generalized geodesic principle[18], we derive analytically the laws of “refraction” and test their validity computationally for different filament orientations. Geodesic is the shortest path that a non-accelerating particle will follow, which in a plane is straight line.

Unlike the refraction of an optical beam, filament refraction appears to be a significantly more complex phenomenon manifesting unparalleled dynamic behaviors. Specifically, at small angles of the filament to the interface, we discovered a diffusion-mediated filament instability and oscillatory regimes, in which one segment of the filament abruptly increases in length, overcoming positive filament tension[25], then gradually shortens to erupt again after several scroll wave rotations. The instability is caused by the gradient force field which is present in the vicinity of the interface and manifests when the filament runs at a small angle to the interface.

CHAPTER 2

METHODS: DYNAMICS OF ARRHYTHMIAS

Computational experiments were carried out numerically using reaction-diffusion equations with Barkley kinetics[26] :

$$\partial_t u = \varepsilon^{-1} u(1-u)[u-(v+b)/a] + \partial_j\left(D_{ij}\partial_i u\right) \quad (1)$$

$$\partial_t \mathrm{v} = \mathrm{u} - \mathrm{v} \quad (2)$$

where *u* and *v* are the activator and inhibitor variable, respectively, and the parameters ε, *b*, and *a* determine the excitability of the medium.

The diffusion tensor D_{ij} was given different values in the lower ($z < 0$) and upper ($z \geq 0$) part of the medium, with a discontinuity at the interface. Specifically, we considered two cases, listed in Table I: isotropic diffusion (Case I) and anisotropic diffusion with a $\pi/2$ rotation of *D* in the *xy* plane (Case II). In the context of cardiac tissue, case II corresponds to a 90° fiber rotation at $z=0$.

Table I. Diffusion tensor for cases I and II.

Case	$D_{ij}(z < 0)$	$D_{ij}(z \geq 0)$
I	$d_1\delta_{ij}$	$d_2\delta_{ij}$
II	$\mathrm{diag}(d_1, d_{2,} d_2)$	$\mathrm{diag}(d_1, d_{2,} d_2)$

The scroll wave was initiated between two hemi-spherical anchors *A* and *B*, located at the lower and upper boundaries of the medium. After equilibration, we slowly (quasi-statically) increased the ratio of the diffusion coefficients (d_1/d_2, see Table 1), progressively increasing the jump in the diffusion tensor at the interface ($z = 0$), until it reached the desired value. The resulting filament had two linear segments [see Fig. 1(a)], whose orientation depended on d_1 and d_2. To investigate the entire range of filament orientations with respect to the interface, we also varied the angle between the filament and the interface by gradually moving one of the anchors.

To compute the filament location we identified the filament tube characterized by reduced amplitude of variable *u* and determined the center of the tube as described in [58]. We chose medium parameters $\varepsilon = 0.02$, $a = 0.9$, $b = 0.05$, which support stable scroll waves with positive filament tension[25]. Medium size was 100 x 100 x 100 nodes with Δx=0.25, for which plane wave speed is accurate within 3%, and no-flux boundary conditions were imposed.

CHAPTER 3

RESULTS AND DISCUSSION: DYNAMICS OF ARRHYTHMIAS

We first apply the geodesic principle[18] to derive the shape of the stationary filament in Cases I and II. According to the geodesic principle, the stationary filament should follow the geodesic with the metric defined as:

$$g_{ij} = (\det D)(D^{-1})_{ij} \qquad (3)$$

The symmetry of *D* requires that the stationary filament consists of two linear segments $\overline{\mathrm{AC}}$ and $\overline{\mathrm{CB}}$ at different angles α and β to the interface [see Figure. 1 (b)]. Let us denote the unit vectors along the segments $\overline{AC}$ and $\overline{CB}$ as $a = (a_x, a_y, a_z)$ for $z < 0$ and $b = (b_x, b_y, b_z)$ for $z > 0$, respectively.

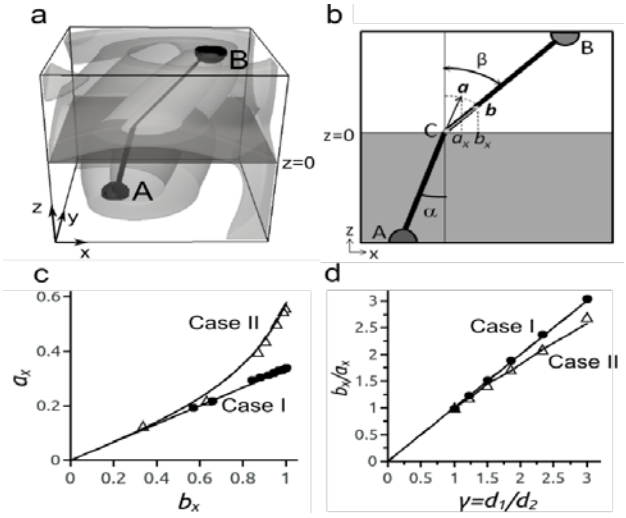

Figure 1: Refraction of a scroll-wave filament in a medium with discontinuous diffusion tensor. (a) Snapshot of a scroll wave and its filament in the model given by Eqs. (1) and (2) (case I: d_1 = 1.5, d_2 = 0.5). The isosurfaces for u = 0.5 are shown in transparent gray, the filament and the anchors in black, and the interface between the upper and lower

halves in transparent dark gray. The filament is noticeably thinner in the upper region because $d_2 < d_1$. (b) Schematic cross section through the anchor plane ($y = 0$) in (a), explaining our notations. (c) Dependency of a_x on b_x as derived from the geodesic principle (lines) and observed in numerical experiments (symbols) for $\gamma = 3$. (d) Numerical verification of Eqs. (6) and (7) for fixed anchor positions and varying γ.

Case I. To find the relationship between α and β, we assume without loss of generality that both anchors are located in the plane $y = 0$. Then, the isotropy of D requires that the whole filament stays in this plane($a_y = b_y = 0$). From Eq. 3 we find the metric tensor g_{ij} for this case:

$$g_{ij} = \begin{cases} (d_1)^2\delta_{ij} & \text{for } z < 0 \\ (d_2)^2\delta_{ij} & \text{for } z \geq 0 \end{cases} \qquad (4)$$

The geodesic condition then can be written as

$$\delta S = \delta \int \sqrt{g_{ij}dx_i dx_j} = \delta \int_A^C d_1 dl + \delta \int_C^B d_2 dl = 0, \qquad (5)$$

from which we obtain the relationship between angles of the upper and lower segments of the filament with the normal [see Fig 1(b)]:

$$\frac{b_x}{a_x} = \frac{\sin(\beta)}{\sin(\alpha)} = \frac{d_1}{d_2} \qquad (6)$$

Equation (6) is reminiscent of Snell's law for light refraction, with the diffusivities playing the role of refraction indices (this filament refraction is markedly different from the refraction of excitation fronts, which follows the tangent rule[27]).

Case II. For simplicity, we again assume that $a_y = b_y = 0$. By applying the geodesic principle, we find that a_x can be expressed as the following function of b_x:

$$a_x = \frac{b_x}{\gamma}(1 - b_x^2(1 - {}^1\!/_\gamma))^{-(1/2)} \qquad (7)$$

where $\gamma = d_1/d_2$. A full technical derivation of this and a more general case of arbitrary fiber rotation will be presented in a future publication. Note that asymptotically at small b_x, Eq. 7 coincides with Eq. 6.

As in the case of light refraction, Eqs. 6 and 7 imply the existence of critical angles α_c for which $\beta = \pi/2$ $(b_x = 1)$. In the context of this study, this means that independently of the anchor's position, the filament will always adapt its shape in such a way that $\alpha \leq \alpha_c$. For Case I, $\alpha_c = \arcsin(\gamma^{-1})$. while for Case II, $\alpha_c = \arcsin(\gamma^{-1/2})$. The solid lines in Figs. 1(c) and 1(d) show the dependence of a_x on b_x and of the ratio a_x/b_x on γ predicted from Eqs. (6) and (7).

To test the validity of Eqs. (6) and (7), we carried out numerical experiments using the full model Eqs. (1) and (2). The values of a_x and b_x were calculated from the filament coordinates using linear regression applied to the lower and the upper parts of the

medium, respectively. The simulation results were superimposed onto the theoretical plots (see Figures 1(c) and 1(d)). In both series of computational experiments we observed excellent agreement with theory.

While holding rather well in a broad range of parameters, the theoretical predictions start failing when $\alpha \to \alpha_c$ and $\beta \to \pi/2$. The deviations were most pronounced in Case I. Figure 2 shows the evolution of the filament as the distance of the anchor *B* from the interface (z_B) gradually decreases. At larger z_B [see Panel (a)], the filament consisted of two rectilinear fragments, in excellent agreement with the theory. When z_B is reduced from $0.77\lambda_z$ to $0.26\lambda_z$, however, the upper segment of the filament deviated from the geodesic and became noticeably curved [see Fig. 2(b)].

As the anchor continued to approach $z = 0$, the deformation increased, and the respective fragment of the filament started oscillating [Figures 2(c)]. The oscillation cycle consisted of two distinct phases: 1) rapid bulging and moving away from the interface, and 2) slow straightening and approaching the interface. The two filament positions shown in Panel (c) represent these two phases. The period of filament oscillations was more than an order of magnitude longer than that of the rotation of the scroll wave. Further reduction in z_B increased the amplitude of oscillation and caused the detachment of the filament from the upper anchor. Attached only at the bottom end, the filament started clockwise precession around the anchor [see Figures 2(d)] until it stopped in a new position (labeled "5") and resumed oscillations.

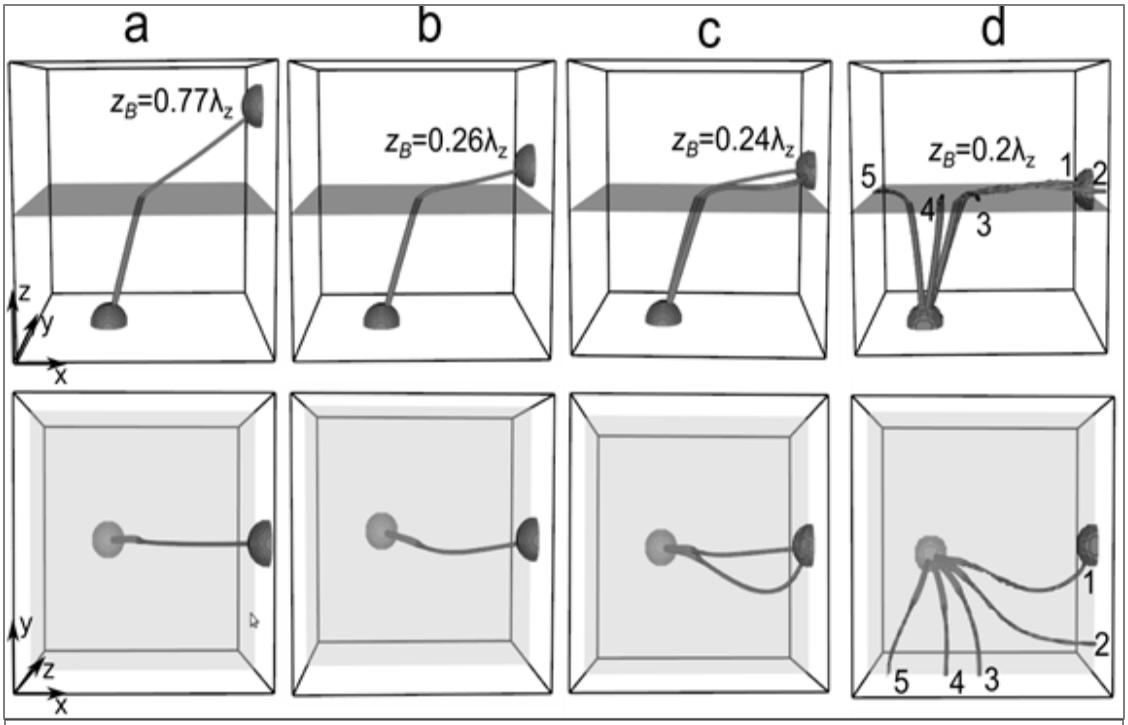

Figure 2: Filament snapshots (lateral and top views) at different anchor positions in case I, with d_1 = 1.5, d_2 = 0.5, (γ = 3). The values of z_B indicate the distance of the anchor B from the interface in units of λ_Z, the wavelength of the scroll wave in the z direction. (a) Filament refraction consistent with the geodesic principle. (b) The upper segment of the filament becomes curved. (c) The filament begins to oscillate in the vicinity of the geodesic solution. (d) The filament detaches from anchor B and rotates in the clockwise direction. The numbers show consecutive filament configurations starting from the moment of detachment.

It is interesting that during these transformations, the filament shape remained close to the geodesic solution. Indeed, the lower segment of the filament remained rectilinear with $\alpha = \alpha_c$. The ratio $\sin(\beta)/\sin(\alpha)$ remained close to γ as prescribed by Eq. (6) (we used linear regression to approximate the curved filament and compute β). The

deviations from the geodesics were less pronounced in case II than in case I (see Figure 3). Within the range of parameters studied, we did not observe any oscillations and the filament remained attached to the lower anchor all the way to $z = 0$.

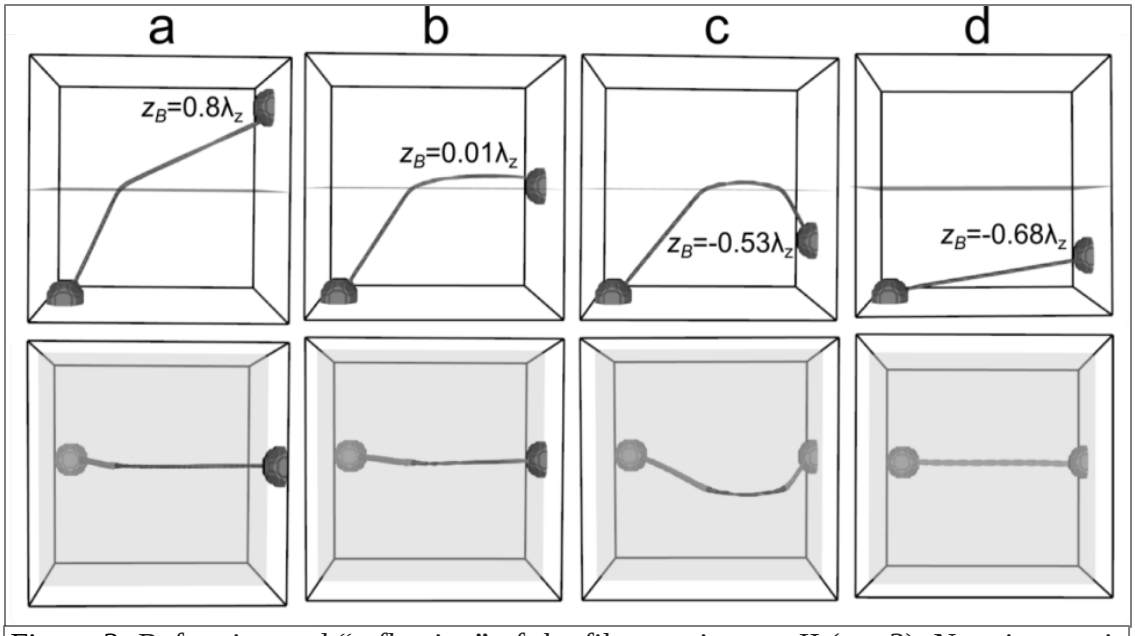

Figure 3: Refraction and "reflection" of the filament in case II ($\gamma = 3$). Notations as in Figure 2. (a) The filament consists of two rectilinear fragments consistent with geodesic predictions. (b) At α close α_c, the upper segment of the filament runs almost parallel to the interface. (c) As the anchor *B* moves below the interface, the filament folds and produces an additional linear segment at an angle close to α_c, reminiscent of internal reflection. (d) Straightening of the filament following further reduction of z_B.

The milder deviations from the theory in case II are due to the fact that in this case only two components of the diffusion tensor change at the interface, as opposed to all three in case I. It would be reasonable to expect that in a generalized case II with fiber rotation at the interface of less than $\pi/2$, the deviation from the theory will be even smaller.

In case II, we observed a phenomenon reminiscent of internal reflection [Figure 3c)]. When we moved the second anchor across the interface to the lower half of the medium, we obtained a filament with 3 segments: The first segment at an angle α close to α_c, the second approximately parallel to the interface, and the third again at an angle close to α_c, (a distant analogy to optical total reflection). When the length of the central fragment became very small, the filament detached from the interface and acquired a rectilinear shape [Figure 3(d)].

The deviations of the filament shape from the geodesic and the complex filament dynamics at small angles to the interface are the result of a short-range force F_b which affects the filament in the vicinity of the boundary separating regions with different diffusion [see Figure 4a]. Such a force is present at any boundary separating domains with different parameters[28] . In our case, $F_b(z) \propto |n \times b|$, where *n* is the normal to the interface pointing in the direction of greater diffusivity. By analogy with two-dimensional cases[28], [29], it is reasonable to expect that the spatial range of F_b is of the order of the filament radius, $w = \lambda_z/2\pi$. Parts of the filament located outside the boundary layer defined by w remain unaffected by F_b [see Figure 4(a)].

The portion of the filament experiencing F_b is therefore w/z_B. For small β the affected portion is small and has little effect on the filament angle. As β increases, so does w/z_B, until the entire segment $\overline{CB}$ is affected ($w/z_B = 1$) as β approaches $\pi/2$. F_b makes the filament drift, while the anchor prevents the end of the filament from moving. This causes the filament deviation from the rectilinear shape and the development of

curvature-related normal and binormal forces which contribute to subsequent filament dynamics[17].

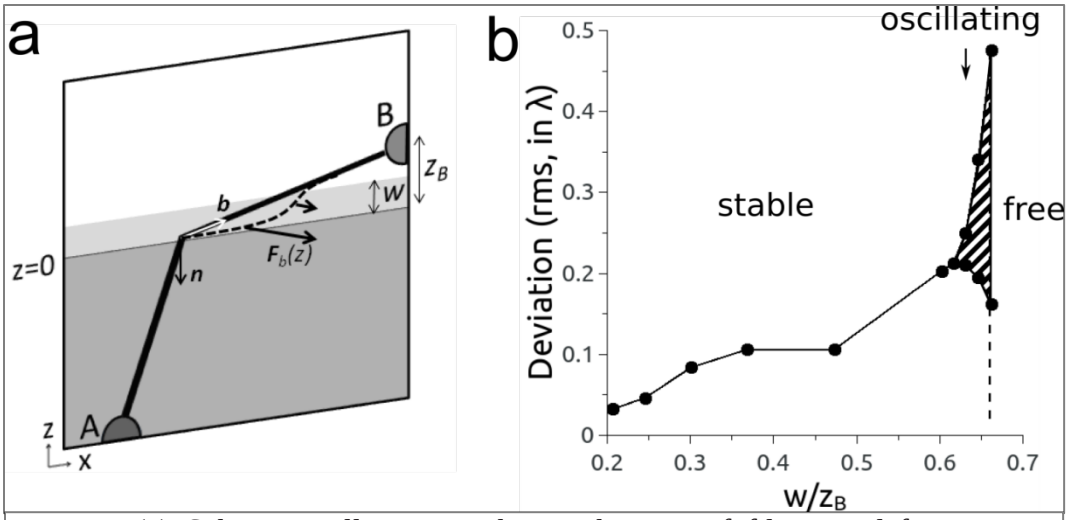

Figure 4 (a) Schematic illustrating the mechanism of filament deformation at small z_B. The portion of the filament inside the boundary layer of width w experiences a force F_b, which pulls it off the *xz* plane, creating a bulge as indicated by the dashed line. (b) Deviation of the upper filament segment from the straight line as a function of w/z_B (case I, γ = 3). Deviation was quantified by determining the distance between the predicted and actual filament coordinates in each cross section (*yz* plane) of the medium and then calculating the root-mean-square deviation. The width of the hatched area indicates the amplitude of oscillations. The dashed vertical line indicates the detachment of the filament from anchor *B*.

Figure 4 (b) shows the average deviation of the filament from straight line as a function of w/z_B for case I. Indeed, the deviation is small when $w/z_B \ll 1$ and dramatically increases as w/z_B approaches 1. Oscillations start as $w/z_B \approx 0.63$, whereas complete detachment occurs at $w/z_B \approx 0.67$. The gradual rise of oscillation amplitude suggests that the bifurcation is supercritical, while the narrow range of w/z_B in which we see deviations is likely the result of the strong dependence of F_b on z.

Our findings have important implications with regard to utility of geodesic principle[30], [31]. The geodesic principle enables the prediction of the shape of the stationary filament exclusively from the diffusion tensor, without considering the kinetic parameters of the medium. The validity of the geodesic principle was proven only for small filament curvatures[32] which limited its practical application. Our study shows that for practical purposes, with the exceptions mentioned above, the requirement of small filament curvature can be relaxed. Computer simulations clearly show that despite significant curvature of the filament near the interface, its shape remains consistent with the geodesic predictions. Considering that this study focuses on the most extreme case of discontinuous diffusion, it is reasonable to expect that the agreement will be even better in the majority of cases where the diffusion changes more gradually.

3.1 Conclusion

In summary, we demonstrated that an anchored filament refracts at the boundary separating domains with abruptly changing diffusivity tensor. In the particular case of domains with isotropic diffusion, the refraction law is reminiscent of Snell's law in geometrical optics. We showed that the condition of small filament curvature used for the derivation of the minimal principle for practical purposes can be relaxed, which significantly extends the utility of the geodesic approximation. Finally, we discovered oscillatory regimes, and instabilities resulting from abrupt changes in anisotropy that shed new light onto the role of the abrupt changes of anisotropy in the development and dynamics of cardiac arrhythmias.

NANOSECOND PULSED ELECTRIC FIELD (NSPEF) DEFIBRILLATION IN LANGENDORFF- PERFUSED RABBIT HEARTS

CHAPTER 4

INTRODUCTION: NsPEF DEFIBRILLATION IN RABBIT HEART

Annually, about 300,000 deaths in the United States occur due to ventricular fibrillation (VF)[33]. The only effective treatment is to deliver high amplitude electric shocks to the heart trans-thoracically using a defibrillator to terminate fibrillation and restore organized rhythm. During the normal cardiac rhythm, action potentials generated by the sinoatrial (SA) node travel through the atria by cell-to-cell conduction. As the activation travels across the atria, it depolarizes the atrial cells resulting in the contraction and pumping of blood from the atria to the ventricles[33]. The activation from the SA node reaches the atrioventricular (AV) node and spreads through the ventricles via a specialized conduction system[34]. This results in the coordinated depolarization of the ventricles which stimulates the contraction of the heart[35], and the electrocardiogram (ECG) of a normal heart is shown in Figure 5A.

VF, in contrast, consists of multiple re-entrant wavelets that depolarize different parts of the ventricles[35], resulting in arrhythmic and ineffective contraction of ventricles[35]. The ECG of a VF episode is shown in Figure 5B; it is irregular with a frequency of 7-10 Hz, much higher normal sinus rhythm, which has a frequency of about 1 Hz.

Figure 5: ECG waveforms in normal and fibrillating heart. Panel A shows the ECG waveform in a normal heart. Panel B shows the ECG waveform during VF

Although the defibrillators currently used are effective in treating ventricular fibrillation, there are reports of damaging effects, like cell damage, pain, cardiac ectopic, tachycardia, arrhythmia, asystole, re-fibrillation, and even death specially due to higher energy shocks[35], [36]. In most cases, more than one shock, and even up to 8 eight shocks need to be applied to terminate disorganized rhythm[37], [38].

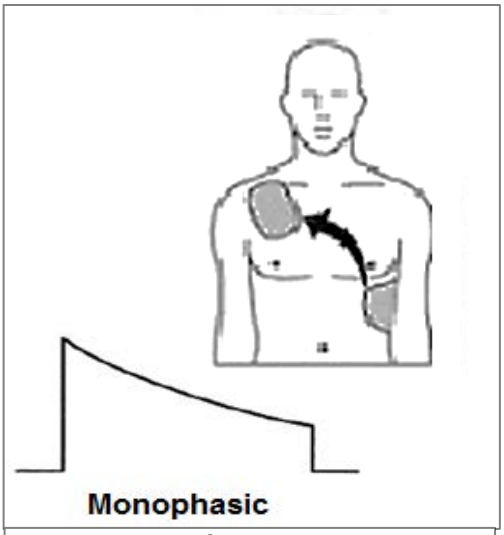

Figure 6: Waveform used monophasic defibrillator along with the paddle position and direction of flow of current.

In the first defibrillators, shocks were generated by discharging a capacitor across the thorax, so that the waveform was a truncated exponential (Figure 6). The typical energy delivered during the application using a monophasic defibrillator is around 400 J[39] and pulse duration is between 5 and 10 ms[40].

Efforts to decrease the amount of energy deposition during defibrillation resulted in the development of shocks with biphasic waveforms, which consist of two consecutive truncated exponentials of opposite polarity (Figure 7)[41]–[43]. Biphasic defibrillators reduced the amount of energy deposited during defibrillation by 20 to 40%, or around 100 J[41]–[44]. Biphasic shocks are now generally regarded as superior and universally used in modern defibrillators[41], [42]. Several papers have tested improvements of biphasic waveforms to further reduce the required defibrillation energy, but achieved only marginal improvements and the clinical benefits of using biphasic waveforms in out-of-hospital patients are also not clear[45], [46].

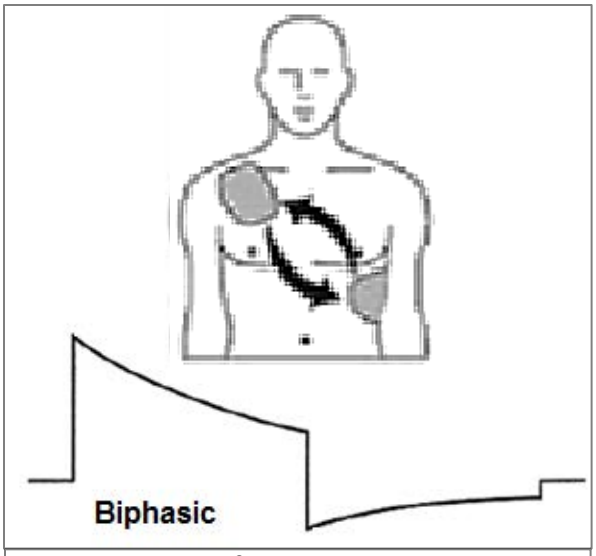

Figure 7: Waveform used in a biphasic defibrillator along with the paddle position and bidirectional flow of current.

4.1 NsPEF defibrillation technology

An interesting, untested alternative to this conventional defibrillation is to apply shocks or trains of shocks of nanosecond duration, also called nanosecond pulsed electric fields (nsPEFs). NsPEFs have been used successfully in other contexts, particularly in tumor ablation[48]. In cancer research, they have also been found to be effective in apoptosis[47] and drug delivery[48]–[50].

Nanosecond PEFs of sufficient strength (approximately 200 mV/ membrane) are known to cause electroporation of the plasma membrane[48]. It has been shown in individual cells that there is a significant range of voltage amplitudes for which electroporation is reversible, i.e. pores eventually reseal and the cells recover. Stronger shocks cause irreversible electroporation and cell death via necrosis. Compared to electroporation that occurs with millisecond pulses, the pores created with nsPEF are smaller[48].

In the case of millisecond defibrillation, resistive currents that charge the cell membranes play an important role in the depolarization of the cells, while nsPEFs being so short, leave little time for capacitive charging and the instantaneous displacement current becomes more important. The greater reliance on displacement current also makes nsPEF defibrillation less sensitive to the presence of structural heterogeneities, so the penetration and uniformity of nsPEFs are better than those of longer shocks[51], [52].

Nanosecond PEFs have not yet been used to stimulate or defibrillate the whole heart, but there are a few studies which demonstrate the ability of nsPEFs to trigger in action potentials in excitable cells. In neurons, it was shown that after nsPEF stimulation, calcium entered the myoplasm and either triggered action potentials or modulated neural activity[53]. Skeletal muscle (gastrocnemius) can also be activated with nsPEFs[54]. In this part of the thesis, we show that nsPEF defibrillation is possible, with defibrillation energies an order of magnitude below the energies typical for millisecond defibrillation.

CHAPTER 5

METHODS: NsPEF DEFIBRILLATION IN RABBIT HEART

5.1 Heart harvest

All animal experiments in this study were conducted in accordance to an approved Old Dominion University Institutional Animal Care and Use Committee protocol. The studies were conducted in an AAALAC accredited facility. The animal was anesthetized in an induction chamber with 4% isofluorane. A toe pinch and ear flick test was done to confirm the animal was in the surgical plane of anesthesia. Once anaesthetized, the animal was placed in dorsal recumbence and the thoracic cavity is shaved followed by an injection of heparin. The thoracic cavity was opened, exposing the heart, and the heart was explanted and moved to a container filled with ice-cold Tyrode solution (128.2 mM NaCl, 1.3 mM CaCl2 (2H2O), 4.7 mM KCl, 1.05 mM MgCl2 (6H2O), 1.19 mM NaH2PO4, 20 mM NaHCO3, 11.1 mM D-Glucose in deionized water, pH=7.35±0.05). The heart was attached to a custom-made cannula and flushed with cold Tyrode solution. Cold Tyrode solution helped in arresting the cardiac activity and prevented deterioration until it was connected to the life-support system. The cannulated heart was Langendorff-perfused with fresh Tyrode solution and then transferred to the experimental setup. A total of 14 rabbit hearts were utilized for this project.

5.2 Experimental setup

Our experimental setup can be divided into the life support system the optical mapping setup.

5.2.1 Life support system

The life support system helps keep the heart alive. The life support system has a chamber that contains the Langendorff-perfused heart. The heart was also superfused with Tyrode solution to maintain ambient temperature at 37+/-1 degree Celsius. The Tyrode solution is aerated with 95% $O_{2,}$ adjusted to maintain pH_{in} the range from 7.35-7.45. The pH- and temperature-stabilized solution is then pumped at a variable rate to maintain a pressure of 50 to 60 mmHg in the heart. We also use an excitation-contraction decoupler, either 2, 3-butanedione monoxime (BDM) or blebbistatin, to remove any motion artifact.

5.2.2 Optical mapping system

The optical mapping system, Figure 8, consists of laser, mirrors, diffusers, filters and a CCD camera. The preparation was stained with the near-infrared dye DI-4- ANBDQBS, with a stock solution made by dissolving 10 mg of dye in 1.2 ml of pure ethanol, made fresh for each experiment. From DI-4-ANBDQBS stock solution, 15 µL of dye was diluted in 15 mL to 20 mL of Tyrode's solution and injected as a bolus. A 1000 mW, 671 nm diode laser (Shanghai Dream Lasers) was directed through a 5-degree conical diffusor and then through a dichroic mirror (λ_{crit}=690 nm) onto the heart to achieve uniform illumination.

Fluorescence light passed the dichroic mirror and a 715 nm long pass filter and was recorded with a CCD camera (“Little Joe”, SciMeasure, Decatur, GA) at 1000 frames per second.

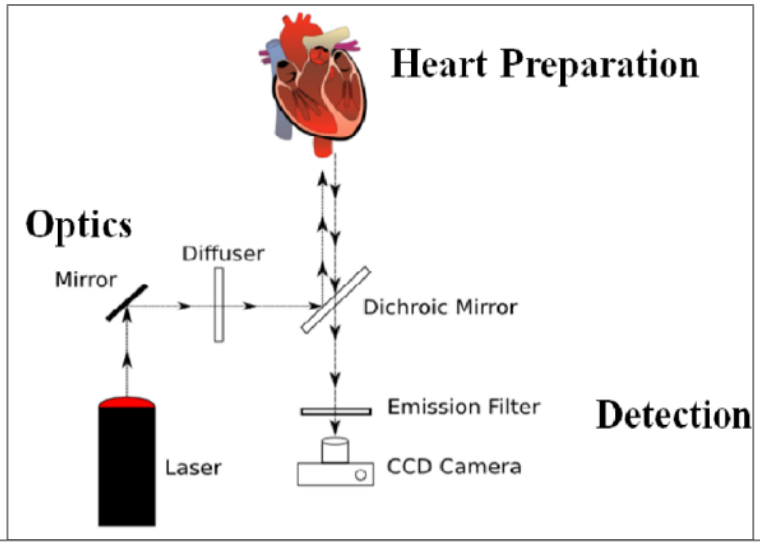

Figure 8: Optical mapping setup consisting of heart preparation, optics and detection. In heart preparation, the heart is continuously perfused and superfused with body temperature Tyrode solution. Optics consists of laser and other optical devices to direct the beam onto the heart. In the detection part, the high speed camera captures the fluorescence.

5.2.3 Mechanism of voltage sensitivity dyes

Voltage-sensitive dyes have a high affinity for the cell membrane and bind to it. The central part of the dye molecule is the chromophore (Figure 9A), which interacts with the light. Photons are absorbed when their energy matches the difference between the energy of the ground state of the chromophore and its excited state.

More precisely, the ground state and the excited state correspond to energy distributions; so that the absorption probability (also called the absorption spectrum) is a continuous function of wavelength (see Figure 9B). Sometime after a chromophore is excited to a higher energy state, it comes back to the ground state by emitting a photon (fluorescence).

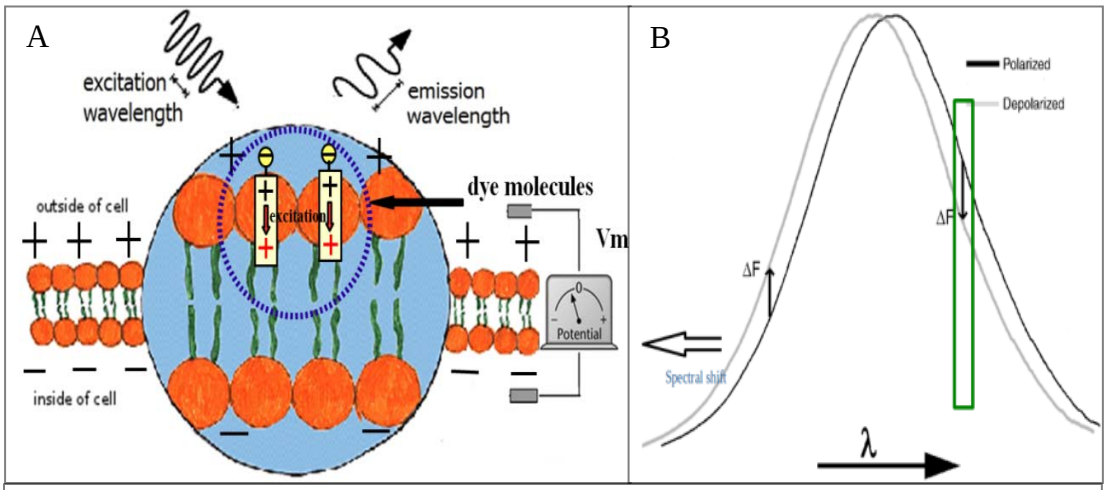

Figure 9: Mechanism of voltage sensitive dye. Panel A shows the schematic representation of voltage sensitive dye molecules (inside the dotted circle). Panel B shows the emission spectrum is shifted as the cardiac cell is depolarized.

Voltage sensitivity of dyes are caused by the fact that the excitation involves the movement of a charge from one end of the chromophore to the other. The dye molecule has parts on either side of the chromophore that ensure that it was oriented with its long axis in transmembrane direction (this is the direction in which the charge moves during excitation). Since the movement of charges in electric fields requires (or yields) energy, this geometry makes the absorption and emission of photons by the chromophore sensitive to the presence of transmembrane voltage. Absorption and emission spectra

shift proportionally to the transmembrane voltage as it changes (Figure 9B). This means that for excitation and absorption of fluorescence at fixed wavelengths, the absorption and emission rates become linear functions of transmembrane voltage; therefore, dye molecules transduce the transmembrane voltage into light.

5.3 Millisecond stimulation

A stimulator functions as a pacemaker that can be used to pace the heart at a desired frequency. Normally, a rabbit heart is paced at 300 ms, with 8 to 10 ms pulse duration, (Grass model SM5E) using monopolar electrode. The stimulation amplitude is set at twice the threshold required to stimulate the heart (typically in the range of 2.5 V/cm to 3 V/cm).

5.4 Temperature measurement and regulation

The Tyrode solution is heated and maintained at $37\pm1^{o}C$ by multiple heat exchangers. The temperature is measured both in the chamber and near the cannula. Depending on the temperature requirements, the water bath temperatures are regulated. The temperature measurements are made using thermocouple elements, which are continuously sampled by a data acquisition board, displayed and recorded.

5.5 Pressure measurement and regulation

A pressure transducer (TD1000, Transducer Direct) was connected very close to the aorta, and the resultant pressure signal was continuously sampled by a data acquisition board, displayed and recorded. The pressure was maintained between 60 to 70 mmHg and was regulated by adjusting the perfusate flowrate.

5.6 Nanosecond pulse generation with transmission line

The stimulation and defibrillation of heart tissue require the delivery of high amplitude nanosecond shocks. The ultra-short rectangular pulse generator, Figure 10, consists of a high voltage DC power supply, a charging resistor R_{charge} to limit the charging current, a transmission line of length L, which acts as a capacitor, and an adjustable spark gap between the charging resistor and the matching resistor Z_M. Once the transmission line is charged to the breakdown voltage, $V_{BD,}$ the spark gap becomes conductive and the capacitor discharges through the load, which is the heart. The voltage on the load V_1 is

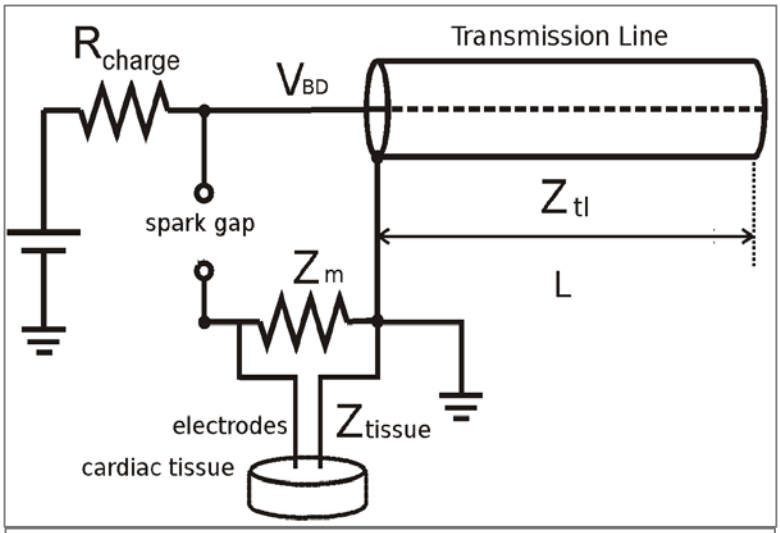

Figure 10: Schematic diagram of a nanosecond pulser.

determined by the impedance of the load Z_l (matching resistor Z_M parallel to the load, i.e cardiac tissue $Z_{tissue)}$ and the impedance of the transmission line, Z_{tl}. If the impedance of the transmission line and the load are equal, then the voltage delivered to the load will be half of the breakdown voltage ($V_{BD}/2$). Thus, by changing the width of the spark gap, we can adjust the breakdown voltage V_{BD}, which will finally determine the amplitude of the rectangular pulse delivered to the cardiac tissue.

The pulse duration of the rectangular pulse is equal to twice the time taken by the electromagnetic wave to travel the transmission line and is given by

$$t = 2\,L/V_p \tag{7}$$

$$V_p = C/\sqrt{\varepsilon_r} \tag{8}$$

C is the velocity of the light in vacuum and ε_r is the relative permittivity of the dielectric material which insulates the transmission line. The transmission line used in our pulse generator is RG-58 coaxial cable with relative permittivity of $\sqrt{\varepsilon_r} = 1.5$. To generate a pulse of 350 ns pulse duration, we used a coaxial cable of length *L*=35 m (350 x 3 x 10^8 x 2 x 1.5). The nanosecond pulse, Figure 11, was attenuated using probe (P6015A, Tektronix) and was recorded using an oscilloscope (Tektronix). In-order to generate rectangular shapes pulse, a matching resistor was connected in parallel to the load. The pulser was pre-adjusted before the start of the experiment to deliver shocks of minimum

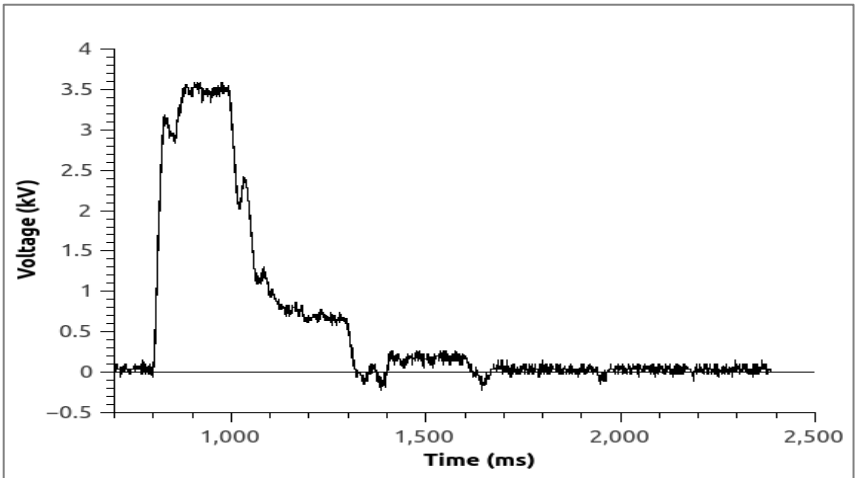

Figure 11: Typical 350 ns pulse used in this project.

of 700 V for cardiac stimulation studies while it is set in the range of 2.3 to 2.6 kV for our defibrillation studies.

5.7 VF induction

In our preliminary studies, inducing sustained VF was one of the most difficult challenges. VF was considered "sustained" if it lasted for more than 30 seconds. Several articles mention that by rubbing the electrodes of a 9 V battery on the ventricles of the rabbit heart for 15 to 20 seconds would induce VF[55], [56]. This method was tried on the first four hearts, but only on a few instances was VF sustained after the battery was taken off. Because of the limited success of this procedure, we also tried placing the heart in between two plate electrodes connected to a 9 V battery. Again, VF was observed as long as the battery was connected but usually stopped as the battery was disconnected. Two other techniques that we found in the literature and tested were "burst pacing"

(inducing VF with rapid pacing with the frequency varying from 8 Hz to 50 Hz) and "incremental pacing", which starts with pacing at 2 Hz and increments every 30 seconds by 1 Hz. These techniques were even less successful than induction with a 9 V battery. Finally, following the recommendations of Dr. Efimov, we decided to add pinacidil (5-20 μMo), a drug that shortens the action potential and in this way makes fibrillation easier to induce, to the perfusate and afterwards jiggle the electrodes of a 9 V battery on the ventricles. The addition of pinacidil greatly facilitated the induction of VF.

5.8 Electrode configuration

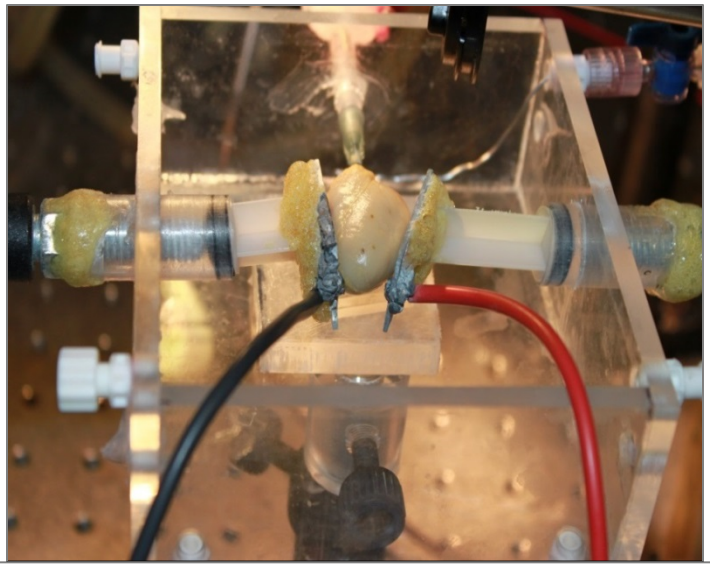

Figure 12: Electrode configuration and chamber. The electrodes are made of aluminum and they are tightly placed onto the heart using screw mechanism.

The electrodes that were used for nsPEF stimulation and defibrillation are made of aluminum and have dimensions of 1.5x3x0.1 cm. The electrodes were initially designed

to be parallel. However, it was observed that the electrodes made limited contact with the heart, especially at the apex, and therefore the shock was mostly delivered at the base. The modified electrodes, shown in Figure 12, were designed to have an angle of 30^{O} at the apex to better approximate the shape of the heart. The electrodes can also be moved laterally, to optimize contact

5.9 Stimulation with nanosecond pulses

During nsPEF stimulation, the heart was not paced with the ms stimulator but allowed to beat in sinus rhythm. The camera was set to record movies (1000 fps) for 3 to 5 seconds and between 1 and 2 seconds the shock was applied. The nsPEF detection system detects the frame in which the pulse was applied and assigns one of the pixels at the top corner with a higher value depending on the applied voltage.

5.10 NsPEF stimulation with indium tin oxide (ITO) electrodes

We also performed nsPEF stimulation with an alternative electrode configuration designed to record the shock-induced activity in the tissue next to the electrode. Note that in the electrode configuration described in Figure 12, the nsPEF shock was delivered laterally and the electrical activity was recorded from the top. In this configuration, it is not known how the tissue closest to the electrode is affected and whether any damaged was being done by the shock. One of the means to study the adverse effect of shock on the cell structure is to study the baseline movement from the side on which the shock was delivered.

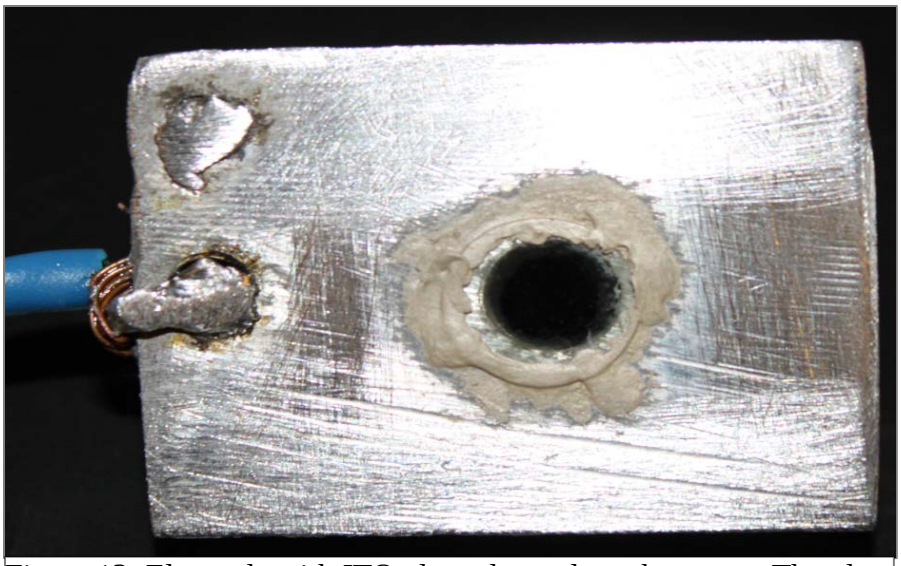

Figure 13: Electrode with ITO glass electrode at the center. The glass electrode is attached with a conductive seal.

To study the baseline shift due to the shock right under the electrode, we used ITO glass electrodes, Figure 13, instead of using regular electrodes. These electrodes consist of glass coated with indium tin oxide, and their special property is that they are transparent even though they have the excellent conductivity associated with metals. A hole of diameter 7 mm was drilled in the center of the metal electrode and covered with the ITO glass electrode using a conductive seal. The electrical contact between metal and ITO-coated glass was confirmed with a multi-meter before the start of the experiment. The electrodes were placed in the line of sight of the camera (rotated by 90° in the clockwise direction compared to the original configuration) and the electrical activity was recorded through the ITO electrode.

5.11 Nanosecond pulse defibrillation

Once sustained VF was initiated, the camera was set to record movies of 3 to5 second duration. After one second, the shock was applied. The movies were saved on a computer, while amplitude of the shock and the name of the movie were recorded manually in the lab journal. A quick evaluation of the recorded movie was done to determine whether the defibrillation was successful or not. If the shock was able to terminate the disorganized rhythm and normal SA activity was observed, we considered the defibrillation attempt successful. One minute after defibrillation, we recorded another movie of one second duration to confirm that the heart was still in sinus rhythm. If necessary, the heart was stimulated with a ms stimulator for few minutes to stabilize the heart before the next episode of VF was initiated. If the shock was unable to defibrillate the heart, the amplitude of the nanosecond pulse was increased by increasing the spark gap distance.

5.12 Millisecond defibrillation

A monophasic millisecond defibrillator that was built using 2 capacitors (10,000 μF), connected in parallel, which were charged through a charging resistor using a power supply up to the desired voltage. For defibrillation, the capacitor terminals are for 10 ms connected to plate electrodes (using solid state relays), so that the capacitors discharged through the heart. We performed millisecond defibrillation in 2 hearts for 7 VF episodes. We started with 40 V for the first two times and the reduced the amplitude to 30, increased to 35 and again tested two 40 V shocks.

5.13 TTC staining

In order to stain the heart, we switched from perfusing with Tyrode solution to perfusing with TTC dissolved in PBS 1%W/V. The heart was perfused with TTC for 15 minutes and preserved in formalin for sectioning. The hearts were then sliced every 2 mm from the apex to 2 mm above the suture.

5.14 Signal and data analysis

Raw movies acquired by the CCD camera (Little Joe, SciMeasure) were filtered with spatial and temporal averaging filters using custom-made software (QT/C++) to have a higher SNR. Afterwards, movies were inverted (i.e. all pixel values were replaced by the maximum possible value minus the pixel value) to reverse the inversion of the electrical signals that takes place during optical mapping (for our filter choices). When we visualized the wave propagation, we linearly transformed every pixel value, so that the pixel values span the entire dynamic range of our system. We have shown data mean ± SD and used Student's t-test when we compare them.

5.15 Activation map

An activation map illustrates the activation sequence of the heart, which enabled us to understand the dynamics of cardiac activation. The algorithm that computes the activation map determines for every pixel when a user-defined excitation threshold is reached and considers the corresponding time as the local activation time. Once the activation times of all pixels have been determined, the times are associated with shades of grey (using black for the earliest and white for the latest activation) and plotted.

5.16 Amplitude Map

An amplitude map shows the amplitude of the action potential for each pixel in the heart. The brighter pixels represent higher action potential amplitudes. The algorithm for determining the amplitude relies on finding the difference between the maximum and minimum (optically determined) transmembrane voltage over the entire action potential.

CHAPTER 6

RESULTS AND DISCUSSION: NsPEF DEFIBRILLATION IN RABBIT HEART

6.1 Stimulation of rabbit heart with nanosecond pulses

We recorded 50 episodes of attempted stimulation in 5 rabbit hearts. In previous ablation experiments, we had shown that nsPEF amplitudes of approximately 10 kV/cm

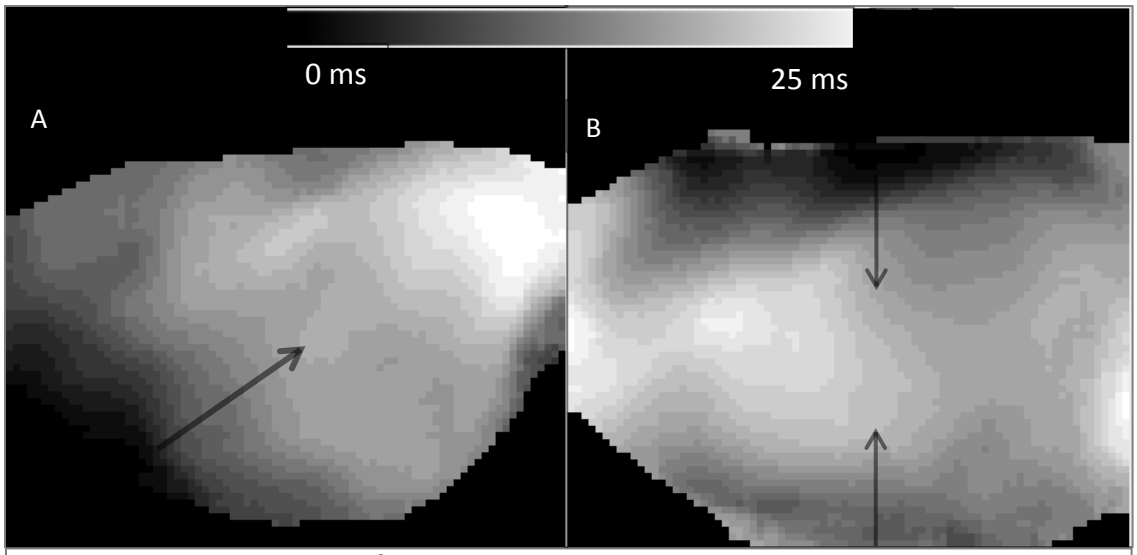

Figure 14: Activation map of sinus rhythm and nsPEF stimulated heart. Panel A shows the activation during to sinus rhythm. The black arrow shows the direction in which the sinus rhythm travels. Panel B shows the activation map after nsPEF stimulation. The arrows in Panel B shows that the activation starts from the two electrodes. The dark shades represent the earliest activation time while the lighter shades of gray shows the latest activation. The time for the activation to travel from the earliest activation to the last activated region was 25 ms.

can be used to ablate cardiac tissue. Since we wanted to avoid ablation, we decided to start with amplitudes far below the ablation amplitude values. We found that shocks below 600V (over 3 cm) never succeeded in stimulating (6 episodes in 3 hearts), while shocks of 1.1 kV or above always succeeded (40 episodes in 6 hearts). In the range from 750 V to 1 kV, stimulation attempts sometimes succeeded and sometimes failed, with the success rate increasing with shock amplitude. This stimulation range was quite broad because in the current pulse generator that was employed, the shock amplitudes were depended on the spark gap distance, and adjusting the gap for desired amplitude was always done by trial and error method. However, from these results, we can conclude that the stimulation threshold amplitude for rabbit heart lies between 750 to 1 kV over 3 cm, the distance between the two electrodes.

The activation maps shown in Figure 14 illustrate the difference between sinus rhythm activation and shock-induced activation. While activation during sinus rhythm (Figure 14A) starts in the lower left corner of the field of view and traverses the heart, shock-induced activation (Figure. 14B) starts from both electrodes, which is expected because shock-induced membrane polarization should be largest near the electrodes. In the five hearts studied, sinus rhythm always produced consistent activation patterns (even though these patterns would differ from heart to heart), while nsPEF activation always started from the electrodes. To assess whether nsPEF stimulation alters the electrical function of the heart, we compared action potential durations for regular activations originating at the sinus node with nsPEF-induced activations. In Figure 15, the action potential duration (APD) that were employed in the nsPEF effect assessment are indicated by black arrows.

Out of the 50 episodes of successful stimulation, we included only those 15 episodes (5 hearts) in the nsPEF effect determination that were performed using electrode configuration shown in Figure 12.

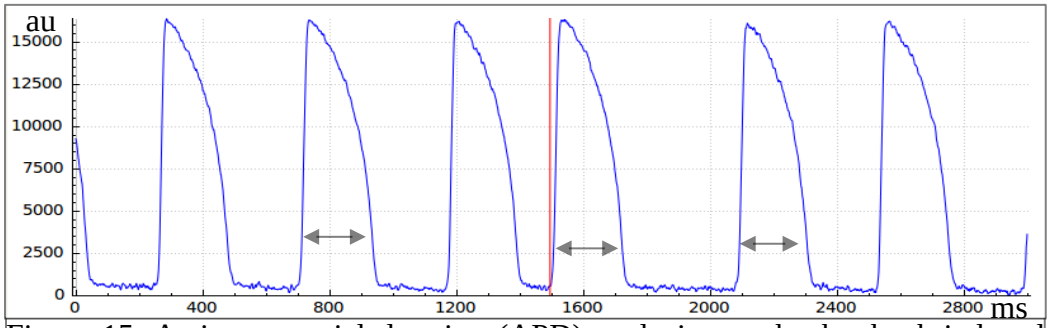

Figure 15: Action potential duration (APD) analysis pre-shock, shock-induced and post-shock for a shock amplitude of 2 kV at 350 nanosecond duration. The red line shows the time at which the shock was delivered. The three analyzed APDs are marked by the black arrow.

6.2 NsPEF stimulation effect on action potential duration

Pre–shock APD (210.87 ms, SD: 6.25 ms) and APD for shock-induced APD (209.45 ms, SD: 2.9 ms) are almost identical. We also studied the spatial distribution of APDs pre-shock, shock induced and post shock (see Figure 16) and did not find any specific spatial patterns in the shock-induced APD distribution.

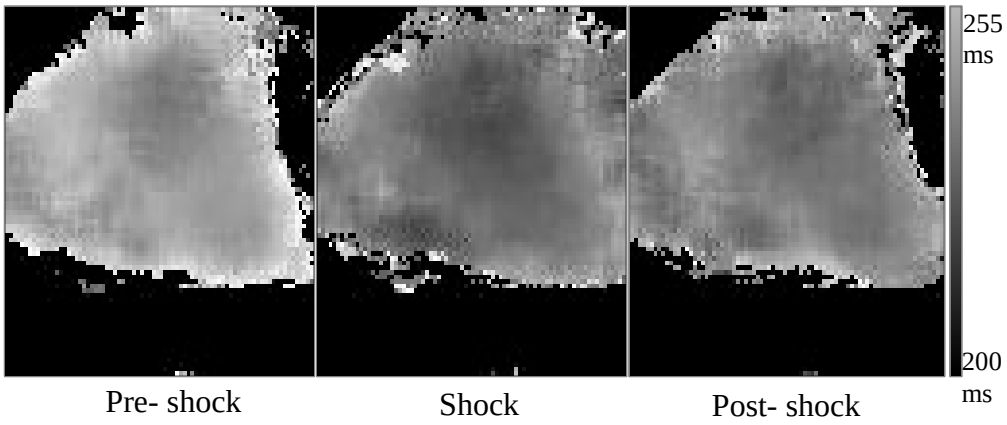

Figure 16: Spatial distribution of action potential duration pre-shock, shock-induced and post-shock.

6.3 NsPEF effect on diastolic interval

The diastolic interval is the time between the end of an action potential and the start of the next one. It is during the diastolic interval that the heart remains relaxed and the

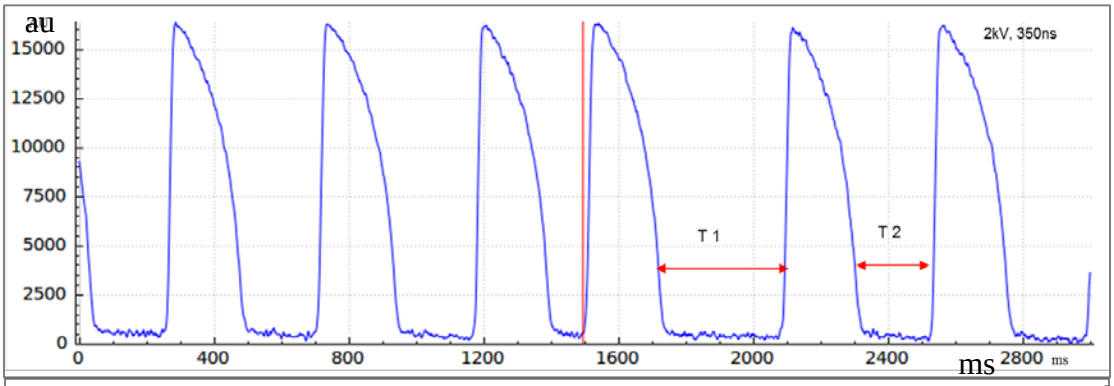

Figure 17: Diastolic interval between acute post-shock and post-shock. The arrival of the shock is marked by the red line. The shock induced an action potential following which the diastolic interval is 50% longer than the following diastolic interval.

chambers of the heart get filled before the arrival of the next excitation. We calculated the diastolic interval pre-shock (i.e. during sinus rhythm), immediately post-shock and second post shock. Figure 17 shows the diastolic interval, immediately post shock, T_2 and second post-shock T_3. We evaluated 12 episodes of stimulation in 4 hearts. Average pre-shock (T_1) diastolic interval was 234.0 ms (SD 3.3 ms), whereas the average post-shock (T_2) diastolic interval was 377.8 ms (SD 1.78 ms). The second post shock (T_3) average was 234.3 ms (SD 2.6 ms). In other words, the diastolic interval directly post shock was always 40 to 50% ($p < 0.05$) longer than the pre-shock and second post-shock interval. The diastolic interval returned to the pre-shock range after the first post shock interval, and the change from pre-shock to second post-shock were virtually identical.

From the data, we can conclude that nsPEF stimulation does have a transient effect on the electrical dynamics of the heart, but this effect appears to pass within a single action potential (about 0.5 seconds).

6.4 Spatial uniformity of action potentials during nsPEF stimulation

To determine whether the shock induced action potentials remain uniform across the heart, we analyzed the action potential amplitude and duration from the center of one electrode to the other electrode (Figure 18A) at every 2 to 3 millimeters (roughly an estimated 10 to 11 positions) in 4 hearts that were stimulated with the electrode configuration shown in Figure 12. Figure 18A shows the 10 positions at which we evaluated the action potentials, marked with black lines. Panels B and C shows the time

at which the shock was delivered (marked by a red line) and the action potentials recorded from positions marked 1 and 2 in Panel A. The APD (Figure 18B) at position marked 1 was 234 ms while the APD (Figure 18B) that at position marked 2 was 238 ms. The average APD from the 10 positions was 235 ms (SD 2.7 ms). The action potential

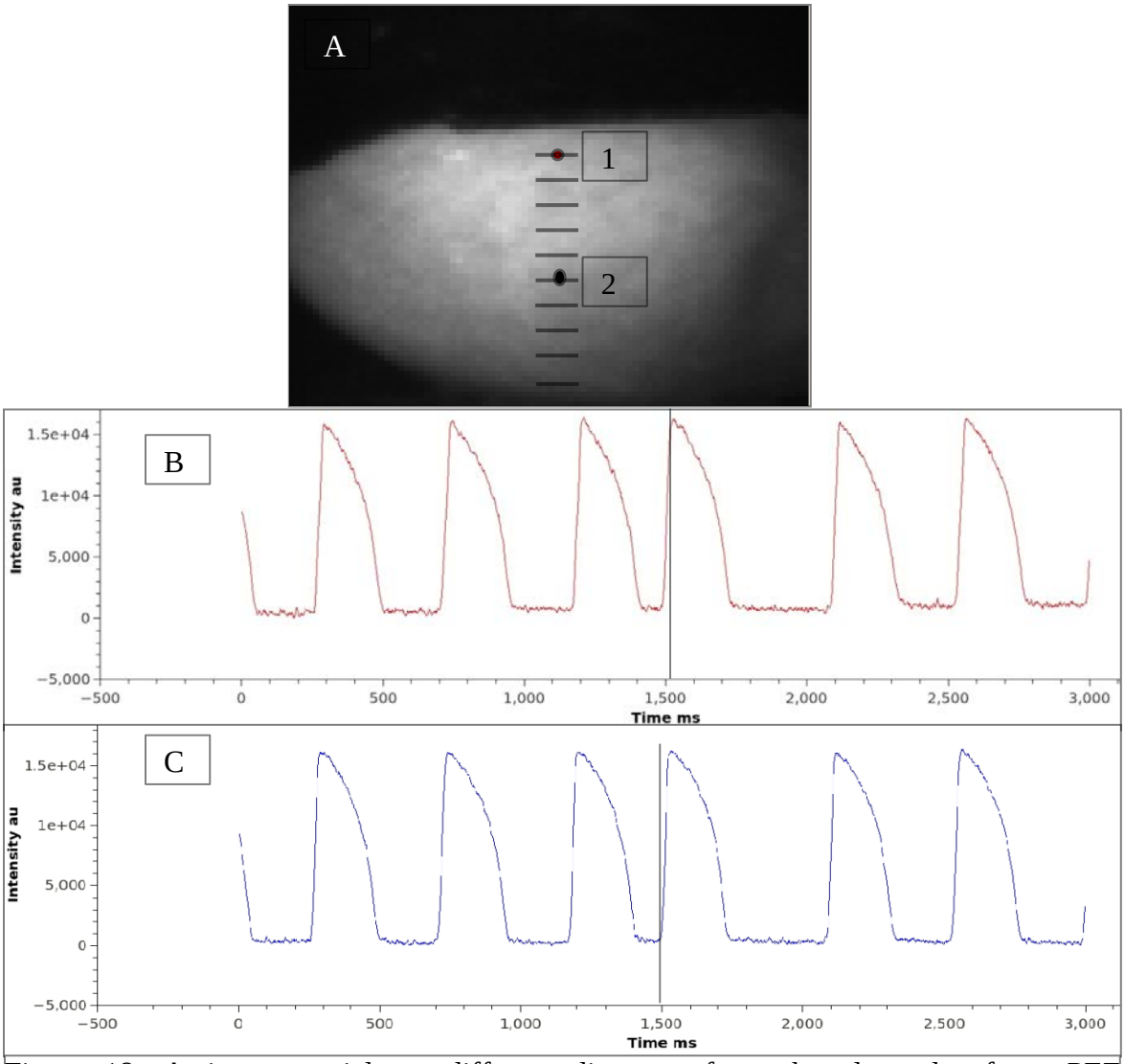

Figure 18: Action potentials at different distances from the electrodes for nsPEF stimulation of a rabbit heart. Panel A shows the 10 recording sites from the surface of the heart. Panel B and Panel C are the action potentials recorded from the 2 location marked 1 and 2 in panel A. Red line shows when the shock was delivered.

duration did not significantly vary over the ten positions ($p < 0.5$). An important implication is that even for the myocardium closest to the electrode, the APD has remained electrically unaffected by the shock.

6.5 NsPEF stimulation indium tin oxide

It is known that defibrillation shocks of sufficient amplitude can result in the electroporation of plasma membrane which in turn can result in serious damage to the tissue[57], [58]. The injury and cell death are a result of the leakage of intracellular components through the compromised membrane, as well the entry of solutes from extracellular medium. Since pores in the membrane also allow ions to pass, electroporation is associated with an upward shift in the transmembrane potential (depolarization). To look for this telltale sign of electroporation, we looked for upward baseline movements of the action potential recordings following the shock. Out of 35 episodes of stimulation using the ITO electrode in one heart, 25 showed no sign of baseline shift. Nine further recordings showed an apparent baseline shift, but only in a narrow ring along the edge for the ITO window. The fact that in the rest of the preparation, no baseline shift could be detected strongly suggests that the shift is really motion artefact; the illumination changes dramatically around the edge of the ITO window, and the shock may be associated with small motions of the heart. In the remaining heart the recording we could not conclusively determine whether a baseline shift occurred. These data suggests that the stimulation with 1.5kV nanosecond shock did not cause serious damage to the cardiac tissue.

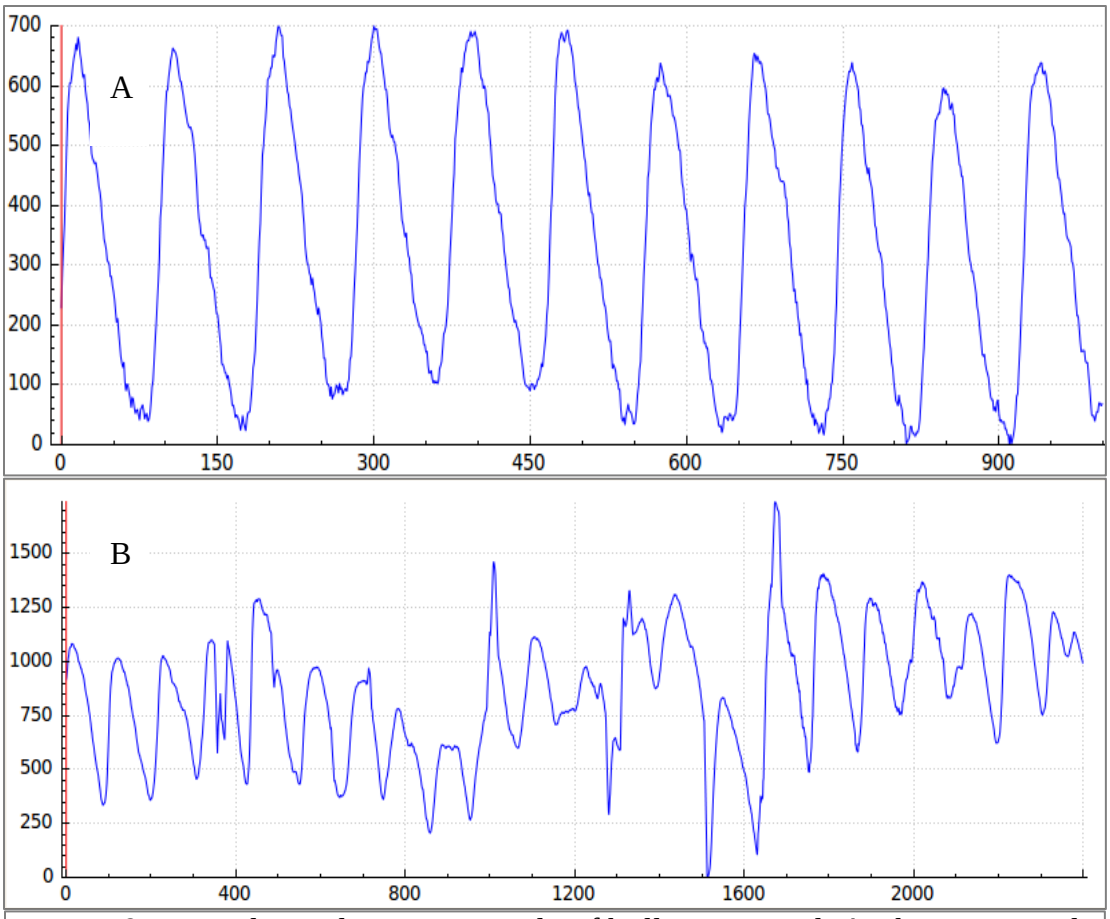

Figure 19: Recordings during ventricular fibrillation. Panel A shows a regular electrical activity but at very high frequency (2 to 3 time faster than normal heart). Panel B shows the ventricular fibrillation. Both types of arrhythmias are considered as ventricular fibrillation for our experiments.

6.6 Reentrant Arrhythmias

Once we were able to stimulate the hearts with nsPEF, we induced reentrant arrhythmias as described in section 3.7. We considered both tachycardia (Figure 19A) and ventricular fibrillation (Figure 19B), because they are closely related (tachycardia indicates the

presence of one reentrant wave, while ventricular fibrillation consists of several such waves) and are typically regarded as equivalent in defibrillation studies. We successfully induced 7 episodes of tachycardia and 18 episode of VF in 10 rabbit hearts. Figure 19 shows the electrical activity recordings during tachycardia and ventricular fibrillation. In case of tachycardia, there is only one reentrant wave, and the frequency of activation is 3 to 4 times faster than normal sinus rhythm as shows in Figure 19A. In case of VF, there are multiple reentrant waves and the electrical activity is also highly disorganized as shown in Figure 19B and any fibrillation which sustains itself for more than 30 seconds after the induction is considered as sustained ventricular fibrillation.

6.7 NsPEF defibrillation

The Figure 20 shows a typical episode of VF followed by a shock of amplitude 2.4 kV marked by red line, and normal sinus rhythm action potential recording. We performed

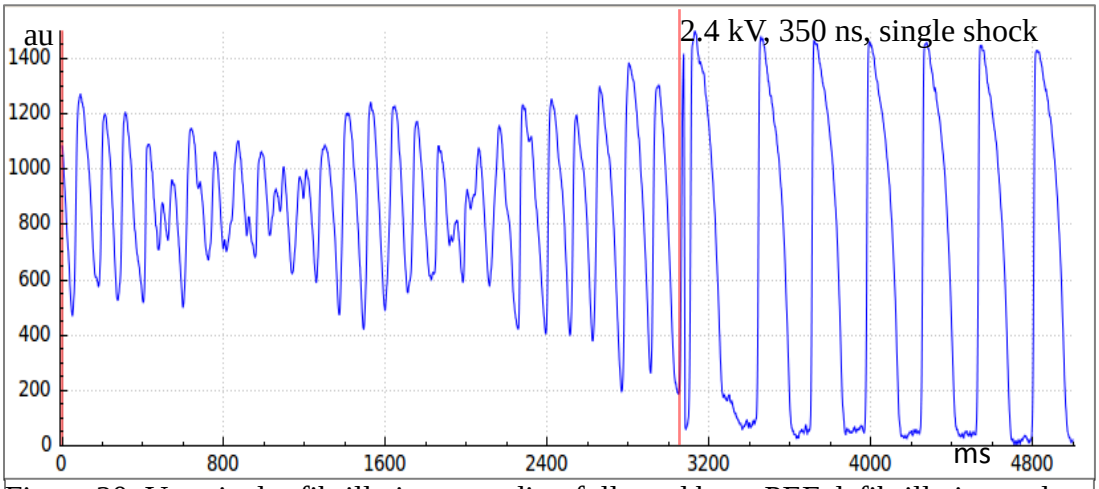

Figure 20: Ventricular fibrillation recording followed by nsPEF defibrillation and normal sinus rhythm.

33 defibrillation attempts of sustained ventricular fibrillation with nsPEF, with shock amplitudes varying from 2.3 kV to 3 kV. Out of the 33 defibrillation attempts in 14 hearts, 25 attempts were successful (75%).

6.8 Defibrillation threshold

Shocks below 2.3 kV never succeeded in defibrillating. The success rate of nsPEF defibrillation with 2.3 kV was 37 % (3 successes out of 8 trials) while for 2.4 kV, it was 62.5 % (5/8). The success rate for amplitude 2.6 kV was 83% (5/6), and for amplitudes above 2.6 kV, we had 100% defibrillation success (11/11). Between 2.3 kV and 2.4 kV defibrillation amplitudes, we had 50% (8/16) successful defibrillation. The defibrillation threshold is usually defined as shock strength that defibrillates the heart 50% of the time[59], [60]; according to this definition, the threshold for nsPEF defibrillation in our experiments lies between 2.3 and 2.4 kV.

6.9 Defibrillation patterns

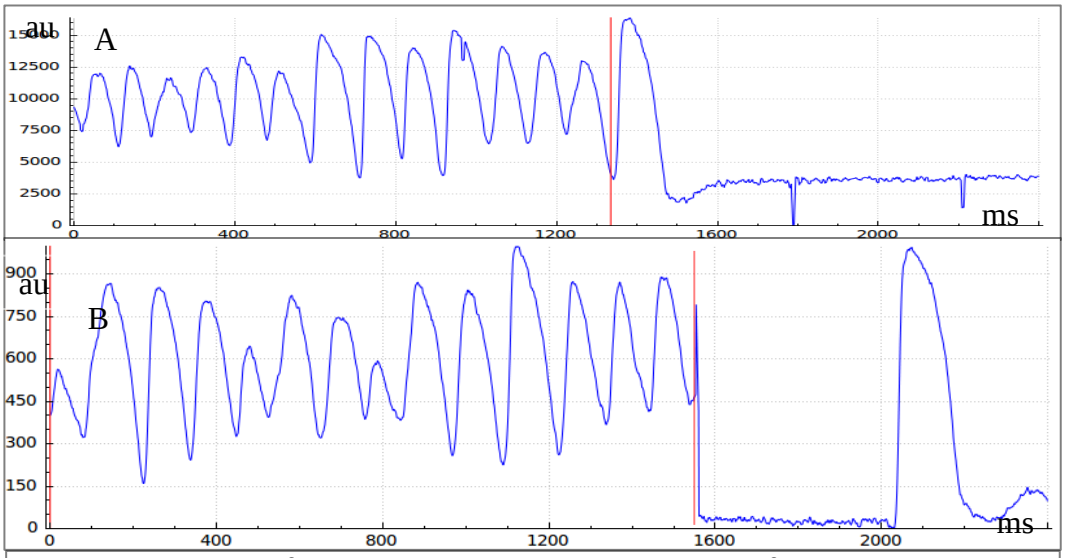

Figure 21: nsPEF defibrillation patterns. Panel A shows fibrillation and shock-induced action potential and then no activity for few seconds. Panel B shows fibrillation and nsPEF defibrillation and sinus rhythm after about 1 second.

We observed 3 different patterns of successful nsPEF defibrillation. In the first pattern, we observed that following the application of the shock, the heart returns to sinus rhythm with a slightly longer diastolic interval immediately after the shock (Figure 20). The second pattern that we observed was that following shock, the heart shows no sign of electrical activity for an extended period of time (2 to 3 seconds) and then returns to normal sinus rhythm (Figure 21A). The movies recorded following such a pattern show that the action potential amplitude and duration were same as before the induction of ventricular fibrillation.

In the third pattern, we observed following the application of shock, the electrical activity halts for about 0.5 second to 1 second and then the heart returns to the sinus rhythm with no significant changes to the amplitude and diastolic interval (Figure 21B).

There were 25 episodes of successful defibrillation with nsPEF. Out of these episodes, 17 exhibited pattern 1, while patterns 2 and 3 exhibited 4 episodes each. As all these patterns were observed for both low amplitudes (2.3 kV) and higher amplitudes (3kV), we cannot conclude that these patterns are associated with certain ranges of shock amplitude.

6.10 NsPEF effect on diastolic interval

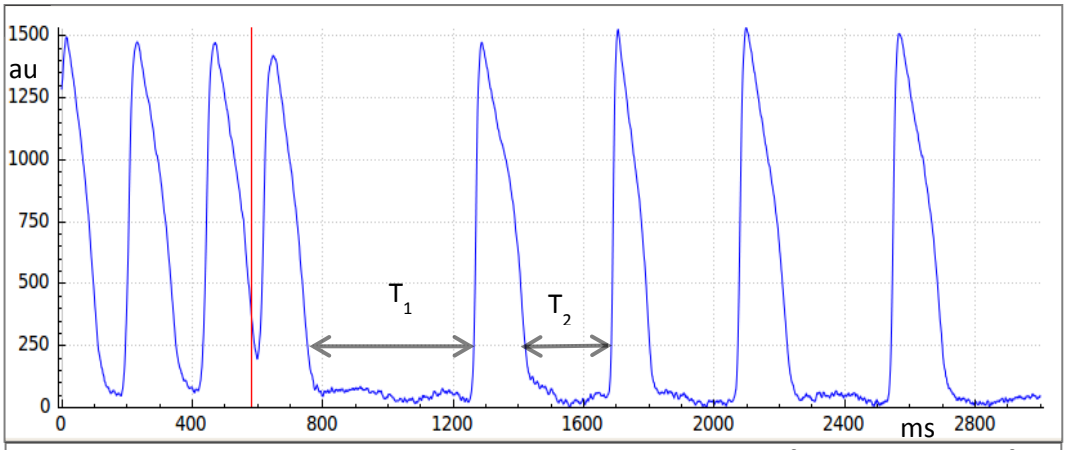

Figure 22: Diastolic interval patterns in nsPEF ventricular defibrillation. The first post-shock diastolic interval is longer than the second post-shock interval.

We also analyzed the diastolic intervals following defibrillation shock, using a similar methodology as in Section 4.3 for stimulation. One difference is that the heart is initially fibrillating, so we cannot evaluate action potential durations or diastolic intervals before the shock.

The diastolic interval immediately after the shock (T_1) was always longer than the normal diastolic interval (T_2, Figure 22). The average first post shock diastolic interval was 425 ms (SD 138 ms) while the average second post shock diastolic interval was 283 ms (SD 112 ms) which was 50 % ($p < 0.05$) longer than the second post shock diastolic interval. The subsequent diastolic intervals were very close to the second post shock intervals. This analysis was performed on the 17 episodes of nsPEF defibrillation pattern 1. The other episodes were not included as they either did not have the first post-shock or second post shock diastolic intervals.

In summary, defibrillation shocks, like the weaker stimulation shocks, have only a transient effect on the diastolic interval (lasting one heart beat).

6.11 No baseline shift following nsPEF defibrillation

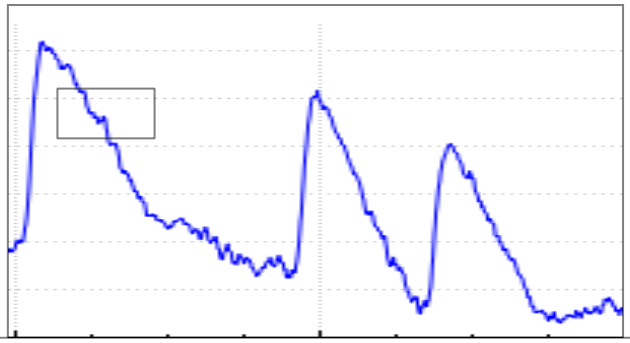

Figure 23: Illustration of baseline shift after a shock application (not from our defibrillation experiments).

As in Section 4.5 for stimulation, we looked for baseline movements of the action potential recordings following nsPEF defibrillation shocks. One difficulty is that since baseline is not reached during ventricular fibrillation, we cannot establish a pre-shock baseline. It is, however, typical that shifts in baseline fade out over the course of seconds (as the heart recovers from electroporation), so that a downward drift of the baseline is observed (Figure 23). We looked for such a downward drift in our 25 episodes of defibrillation in 14 rabbit hearts, but never observed this sign of electroporation.

6.12 Tetrazolium Chloride (TTC) stain

TTC staining is a technique that can be used to differentiate the viable tissue from non-viable ones. The colorless TTC enzymatically turns to a red formazan product in metabolically active cells, while dead tissue remains unstained. In our experiments, if there was any tissue damage due to the nanosecond shock, it should occur rather at the electrodes than towards the center. We performed TTC staining on one heart (see Figure 24). In this experiment, we had applied a single 2 kV shock, a single 2.3 kV shock, one double 2.3kV shock, one double 2.6 kV shock, and three single 2.4 kV shocks. In this heart, TTC staining did not reveal any dead tissue near at the electrodes. However, we did observe some areas of the septum which remained unstained, but we believe that this was not caused by the shock but by problems associated with the perfusion of the tissue.

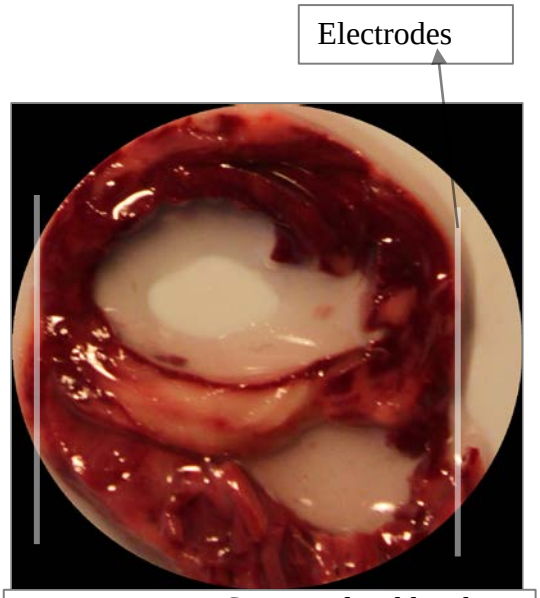

Figure 24: TTC stained rabbit heart. Cross section of the heart stained with TTC. The 2 white lines show the position of electrodes.

6.13 Millisecond defibrillation

The standard way of defibrillation is to deliver a millisecond shock (Figure 25) directly to the heart. We used the standard defibrillation as a control against the nanosecond pulse defibrillation. We performed millisecond defibrillation on 2 animal hearts for 7 VF

episodes. The first two 40 V (Figure 25) shocks successfully defibrillated (Figure 26) the heart. In order to determine the threshold of millisecond defibrillation, we reduced the amplitude to 30 V.

The 30 V shock failed to defibrillate the heart and therefore the shock amplitude was increased to 35 V which successfully defibrillated the heart. The 35 V shock defibrillated the heart 50% of the time while the 40 V shock had higher success rate of 75%. This data suggests that the threshold for millisecond defibrillation is approximately 35 V over 3 cm (distance between electrodes), but more experiments are necessary to establish a precise value. A sample action potential recording during a millisecond defibrillation is shown in Figure 26. The time at which the pulse is delivered is marked by the red line (Figure 26).

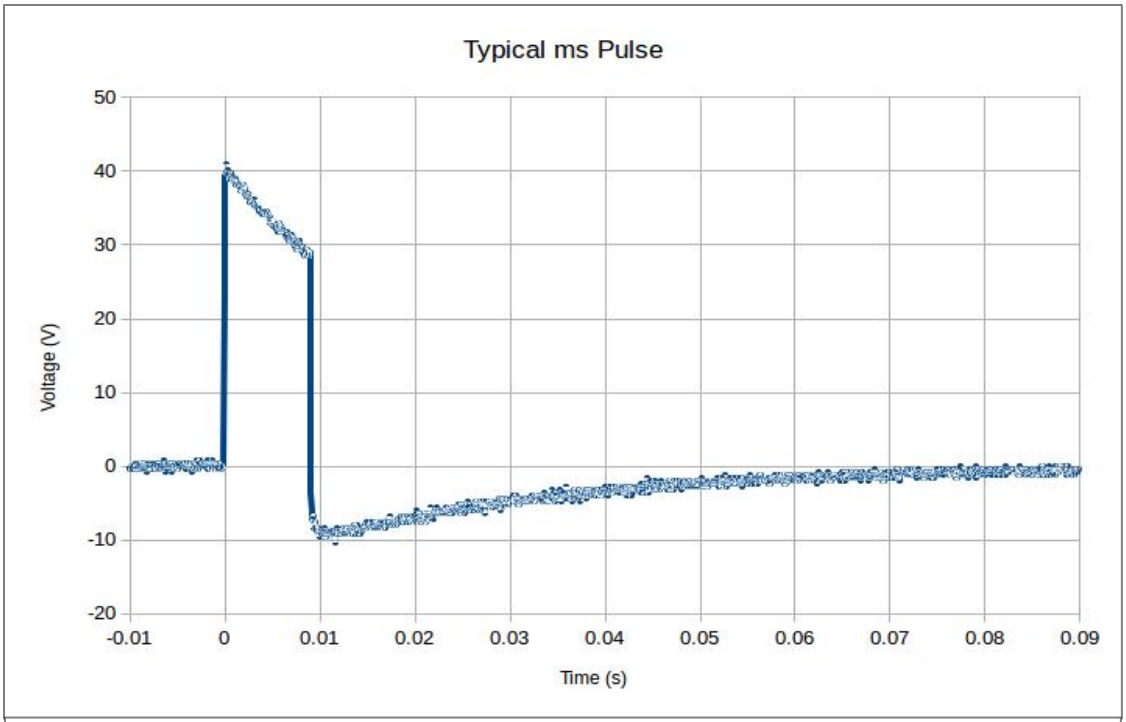

Figure 25: Typical ms pulse used for defibrillation (10 ms pulse duration).

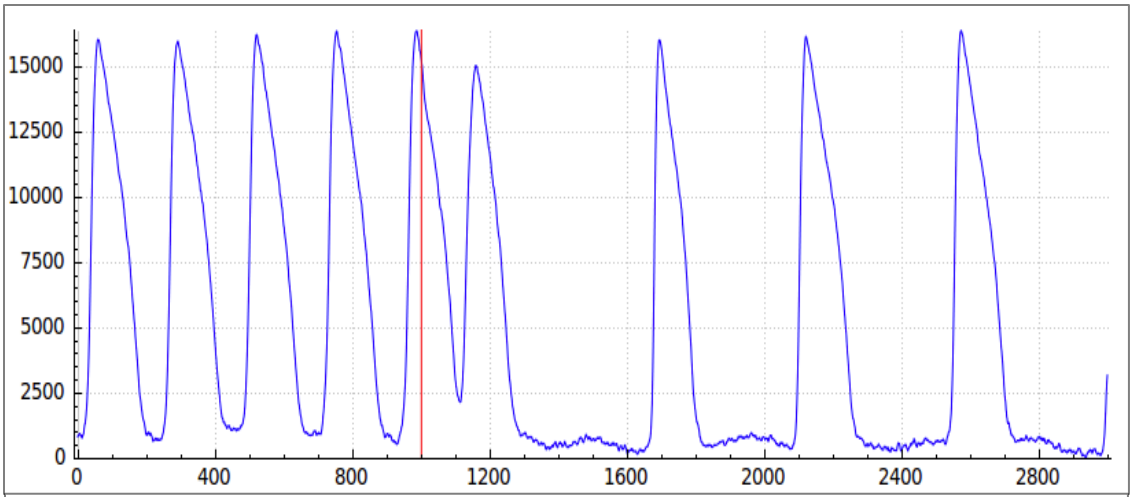

Figure 26: Action potential recording during ms defibrillation. The time at which the shock is delivered is marked by a red line. The shock induces an action potential after which sinus rhythm is observed.

6.14 Energy required for nsPEF and ms defibrillation

Since we are interested in comparing the energies required for millisecond and nsPEF defibrillation, we measured current flowing through the circuit during defibrillation is recorded using a Pearson probe. The energy required to defibrillate the heart during the five episodes of defibrillation is then calculated using the equation:

$$E = \int_0^t U(t)V(t)dt \qquad (9)$$

It was found that the energy required is around 530 ± 80 m J in 5 episodes of ms defibrillation which is consistent with the literature values.

Since energy was an important reason for the development of nsPEF defibrillation. The nsPEF energy was calculated using the equation:

$$E = \frac{1}{2} C U^2, \;\; c = 21.2\, nF \tag{10}$$

The calculated energy for defibrillation is found to be E=64 ± 7mJ.

In comparison to the ms pulse, where energy deposited at the threshold is 530 ± 80 mJ (n=5), the ns pulses reduce the deposited energy by a factor of approximately 8.

6.15 Conclusion

We showed that nsPEF can be successfully used to stimulate and defibrillate rabbit hearts. The nsPEF amplitude required to stimulate rabbit hearts lie in the range of 0.75 to 1kV for a distance of 3 cm. The action potential recording also showed that the application of nsPEF did not affect the heart electrophysiologically in terms of action potential duration and diastolic intervals. The myocardial damaged assessed by TTC staining did not see tissue damage, especially close to the electrodes where the effect if any, should have been more visible. We also showed that the energy required to defibrillate the rabbit heart is eight times less than the ms defibrillation energy.

EFFICACY OF INJECTABLE THERAPEUTIC AGENT IN PROMOTING REGENERATION OF INFARCTED TISSUE IN RAT HEARTS

CHAPTER 7

INTRODUCTION: TA-TREATED RAT HEARTS

1 out of 4 deaths in a year, that is 600,000 in the US, is caused by heart disease, and half of these deaths are attributed to coronary heart disease[61]. The most serious form of coronary heart disease is myocardial infarction (MI). It occurs when a coronary artery is so severely blocked that there is a dramatic reduction or complete disruption of blood supply, causing damage or death to the territory of the myocardium (heart muscle) that was supplied by the blocked coronary vessel (see Figure 27)[62], [63] . The coronary vessel gets blocked due to plaque buildup called atherosclerosis and/or by a clot (e.g. of coagulated blood) that obstructs the flow of blood in the vessel[62] (Figure 27).

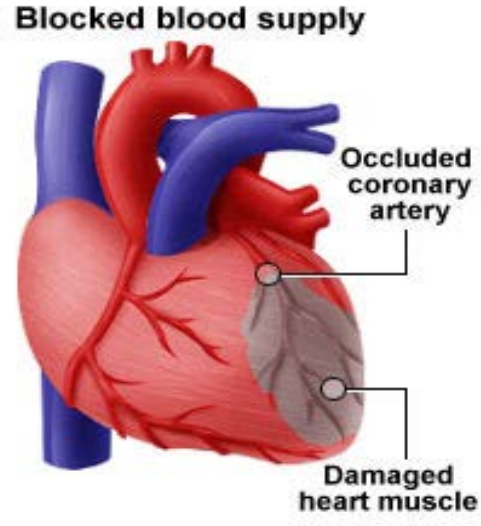

Figure 27: Heart with myocardial infarction.

7.1 Pathogenesis of myocardial infarction

Following MI, affected tissue undergoes an initial inflammatory phase, to up-regulation of matrix metalloproteinases (MMPs) that progressively degrade the extracellular matrix (ECM), causing the realignment of myocyte bundles and individual myocytes, which leads to infarct expansion and heart wall thinning, and finally to a collagen scar being deposited to prevent ruptures and deformations of the myocardium[64]. The myocardium is unable to restore its original cellular and extracellular matrix composition, that results

in the left ventricular (LV) remodeling. LV remodeling is the resizing of ventricular size, shape and function due to mechanical, hormonal and genetic factor[65], [66]. The remodeling can happen during normal growth to adapt to physiological changes or can be pathological due to cardiac vale disease, cardiomyopathy or myocardial infarction[65], [66]. This is seen to progress to cardiac dysfunction and eventual heart failure[64]. Heart failure typically necessitates a heart transplant or LV assist device, the only currently available treatments. Thus, there is a need to develop new and effective treatment that could regenerate infarcted tissue and prevent the development of heart failure.

Recently, a number of approaches using regenerative medicine have gained significant attention in treating heart disease. Some of the approaches use cellular therapies and gene therapies while there are also developments using extracellular matrix derived biomaterials with some degree of success. Bone marrow cell based therapies are used in trials to stop the progression of ischemic cardiomyopathy and congestive heart failure but with have limited success, however cardiac progenitor cells were found to be more promising in regenerating myocardial tissue following infarction[67], [68]. Cell therapeutics using autologous cells in regenerative cardiac treatment have donor-to-donor variability which makes treatment more complicated.

In many studies, it was observed that the injection of cells at the site of injury have further complicated due to the difficulties in retention, integration and survival of the cells at the injection site[69]. These observations and the paracrine effects of the cells to

led to the use of biomaterial scaffolds such as ECM and growth factors for delivering cells to the infarcted region[69].

Biomaterials like Matrigel derived from basement membrane rich matrices and pig muscle-derived matrices have been found to be promising in regenerating infarcted and ischemic tissues by promoting angiogenesis and preventing remodeling of LV in rats and porcine models[69], but murine sarcoma-derived Matrigel is found to be problematic for human interventions, and porcine matrices are found to under-perform compared to human-derived matrices[70]. There are also risks involved in using animal tissue in humans like immune rejection due to the presence of cell particles, DNA and other remains of ECM from animal tissue.

In this study, we tested a newly developed injectable therapeutic agent (TA). Due to non-disclosure agreements (NDA) signed, we are not able to describe the motivation of the approach or the composition of the TA.

7.2 Development of experimental model

In rats as in humans, sufficiently large infarctions typically develop over time into heart failure[71].This made rats a preferred infarct model, and we chose it for this study as well.

It is known from the literature that the myocardial infarction models in small rodents are challenging, with low survival rates of about 50%[72]–[74]. Also, this was the first study

involving survival surgery that our lab embarked on. Keeping this in mind, we initially designed the study into 2 cohorts, the first to test and validate our surgical approach and the second for myocardial treatment with TA. In the first cohort, the goal was to master the infarction model animal surgery with at least 50 % survival. As we started with the surgeries, this proved to be an ambitious goal. The challenges faced in the first cohort started with intubation to sedate the animal. The small size of the larynx made it hard to visualize the tracheal opening while inserting the catheter, and the intubation catheter can easily become inserted into the neighboring esophagus by accident. The procedure was made further complicated since multiple unsuccessful intubation attempts caused laryngospasm glottic and local tissue trauma. Also, if the rat was not successfully intubated in the first few attempts, the animal would regain glottic reflexes, which made subsequent intubation attempts even more difficult. Our surgical approach further required an intravenous line, which was difficult to place in the small veins of our rats. It was also challenging to ligate a branch of the coronary artery to create myocardial infarction without causing substantial blood loss during or after the surgery (due to the small size of the rat heart). Due to these difficulties and the low success rate, we decided to consult with Dr. Salloum from Viginia Commonwealth University, who is an expert in small rodent surgery and has performed more than 3000 myocardial infarct surgeries in small animals successfully. Following the visit to Dr. Salloum's laboratory, the surgery procedure was modified (see chapter 6) with the addition of another cohort to the study thus increase the study groups to three. In the second cohort, we established the new surgery procedure. The third cohort was used to study the efficacy of TA in treating infarction.

CHAPTER 8

METHODS: TA-TREATED RAT HEARTS

8.1 Myocardial infarction model

All animal experiments in this study were conducted in accordance with an approved Old Dominion University Institutional Animal Care and Use Committee protocol. The studies were conducted in an AAALAC accredited facility. The animal surgeries are divided into three cohorts. The goal of cohort 1 study was to establish the surgical procedure. This procedure was performed on 9 Sprague Dawley male rats whose weight was in the range of 450 gms to 500 gms. The animals were anesthetized, shaved, weighed, and echocardiography performed 2 days prior to the surgery. On the day of surgery, each animal was anesthetized with 3% isofluorane, injected with ketamine (50 mg/ml, 0.68 ml) and xylaxine and intubation was performed with a 16 G catheter through the mouth into the trachea. The catheter was connected to a ventilator and the rat was ventilated with isofluorane at 2.5% and 400 ml/min oxygen. The stroke volume was set at 3.4 ml and 75 strokes per minute. Just before surgery, amiodarone (an anti-arrhythmic) was injected to decrease the cardiac sensitivity. The animal was placed on a heating pad and prepped by alternate swabbing with betadine and 70% isopropyl alcohol (IPA) (3 times each) and then draped. Ophthalmic ointment was applied. Once intubated, we performed a left thoracotomy (2-3 cm) in the third or fourth intercostal space to access the heart. The heart was pushed up with the side of the left anterior descendant (LAD) branch of the coronary vessel pointing towards the surface to access the heart by placing sterile cotton gauze soaked in the saline underneath the heart and by using cotton swabs. Any blood in the chest cavity was wiped so as not to cloud the coronary artery. Once the heart was in

place, the distal branch of the LAD was located and a stitch was made with 5-0 silk to ligate the vessel. It was also made sure that the needle did not pierce too deep to penetrate the chambers. The retractors were released and the opening was covered for 30 minutes with sterile gauze soaked with saline to prevent the tissue from drying. The 30 minute window mimics the conditions in human assuming that it takes about 30 minutes for the patient to reach the hospital following the onset of symptoms of heart disease. At the end of 30 minutes, the retractor was placed again and saline was used for control injection, 0.075 ml divided between 4 sites around the ligated vessel was injected. The needle was bent at the tip so as to make sure that the needle does not pierce all through the myocardium into the ventricles. During suturing, the isofluorane was reduced, from 2.5 to 1.5% while the muscle was sutured and to 1.0% while the skin was sutured. When suturing was complete, the ventilator was disconnected. When the animal showed the first signs of waking, facial twitches and tail movement, the intubation tube was removed and the animal moved to a clean housing cage on the heating pad. The pleural cavity was closed, using 4-0 vicryl for all 3 layers: four interrupted stitches were used to close the ribs, 5 running stitches to close the muscle layer and 9 interrupted stitches to close the skin. Phenylephrine (anti-hypotensive) was injected whenever there was a drop in blood pressure. Lidociane (a vaso-antispasmatic) was given continuously via an IV drip to prevent vascular spasms during the surgery. Rimadyl (carpofen) tablets were added to the cage every day for the next 3 days whenever the animal survived the surgery.

In the second cohort, 8 more animal surgeries were performed on the basis of the procedure observed in Dr. Salloum's laboratory at Virginia Commonwealth University, VA. Dr. Salloum has performed more than 3000 small rodents including mice and rats survival surgeries. Dr. Salloum did not use any drugs to other than isoflurane (to anesthetize the animal). His intubation technique relied on illumination of the larynx through the tissue of the throat, thus avoiding that the intubation tube would cast a shadow on the vocal fold. Dr. Salloum also pointed out what exactly we needed to look at in the view down the mouse's throat, and showed us how with experience, the intubation can be done reliably in seconds. The entire infarction surgery took only about 3-5 minutes, as opposed to the 1-2 hours our more complex procedure had taken.

As before, the animals were anesthetized, shaved, weighed, and echocardiography was performed 2 days prior to the surgery. In these set of experiments, the animals were anesthetized and intubation with a 14 G catheter was performed while the animal was laid in supine position on a intubation stand and the larynx illuminated from outside. Amiodarone and phenylephrine were no longer used during the surgery. Rimadyl (carpofen) tablets were added to the cage every day for the next 3 days whenever the animal survived the surgery.

In cohort three, we used TA to test the efficacy in treating myocardial infarction in rat hearts. Sixteen Sprague Dawley male rats (~500 g) were purchased from Harlan Laboratories (Indianapolis, IN). Animals were allowed a 48-hour acclimatization period and were given a course of prophylactic antibiotic 2 days prior to surgery. Induction of

anesthesia was initiated with 3-4% isoflurane inhalation and an intramuscular injection of acepromazine at 1 mg/kg. Intubation was performed with a 16G intravenous catheter, and animals were ventilated with a volume-controlled ventilator at 8-10 ml/kg tidal volume at 70 breaths per minute. 2-3% isoflurane was used to maintain anesthesia. A heating pad placed underneath the animal was used to support body temperature throughout the procedure. Animals received a prophylactic 14 day antibiotic course of trimethroprim sulfate at 0.5 mg/kg daily, and sterile technique was utilized to prevent infection.

Electrocardiogram (ECG) leads were placed on the right and left side of the animal's thorax and monitoring of the ECG was performed throughout the procedure and recorded for analysis. The heart was surgically exposed with a left thoracotomy at the fifth intercostal space. Pericardial removal exposed the left anterior descending (LAD) coronary artery. LAD coronary artery occlusion was performed with a 5.0 silk suture to induce ischemia in the distal regions of the left ventricular myocardium. Observation of blanching of the myocardium was used to confirm induction of ischemia, along with ECG monitoring. Treatment with TA or sham (saline) injections was initiated thirty minutes after the induction of ischemia, in order to ensure myocardium death in the ischemic region prior to injection. During this time thoracic cavity was left exposed, but covered with moist gauze to minimize dehydration and infection. Following injections, the thoracic cavity was closed with 4-0 vicryl suture. The lungs were momentarily fully inflated to expel any air trapped in the thoracic cavity prior to sealing the cavity to prevent pneumothorax. The remaining muscle, connective and skin layers were then also

closed with 4-0 vicryl suture in an interrupted pattern. Pain was controlled with carprofen and buprenorphine for at least 48 hours until no longer needed.

8.2 Echocardiography

Echocardiography was performed 2 days prior to the surgery and twice post-surgery, at 4 weeks and 8 weeks, on all control and TA-treated rats using a Vevo-770 (VisualSonics) with a 13-23 MHz non-linear array transducer. Each rat was anesthetized with 1.5–2.0% isoflurane by mask, the chest was shaved, the animal was laid in the supine position on a warming pad (Sunbeam). Two dimensional M-mode and B-mode data were recorded in parasternal long and short axis. All data were analyzed offline with ultrasound machine software at the end of the study. All echocardiogram measurements were performed using the same equipment and by the same examiner. The examiner was not aware whether the rat under examination was TA-treated.

8.3 Treatment of ischemic myocardium

TA was warmed to room temperature prior to injection into the myocardium. Thirty minutes post-ligation, three injection sites in the ischemic myocardium were chosen based on the location of blanching, indicating the ischemic region. Each treatment site received 25 μL of TA for a total of 75 μL. No backflow of TA was observed. A sham control group received vehicle only injections, which were 0.9% saline, per the injection strategy.

8.4 TA remains at the site of injection

An important question is whether the TA that we injected remains at the injection site or flows back out of the tissue once the needle is remove or would flow back due to the muscle resistance. This was important to know because, the whole study was hypothesized on the basis that TA remains at the site of inject and plays the major role recruiting the cardiac stem cells and promoting angiogenesis at that site of injury. We confirmed that the TA remains at the injection site, but because of an NDA, we are not able to provide the details here.

8.5 Optical Mapping

8.5.1 Heart harvest

Eight weeks after the initial surgery, hearts were extracted and their electrical activity was analyzed with optical mapping[35]. Each animal was brought to a surgical plane of anesthesia with 3-5% isoflurane and injected with 1 IU/g heparin. Bilateral thoracotomy was performed to expose the heart. The heart was then excised and immersed in ice-cold Tyrode solution (128.2 mM NaCl, 1.3 mM $CaCl_2$ ($2H_2O$), 4.7 mM KCl, 1.05 mM $MgCl_2$ ($6H_2O$), 1.19 mM NaH_2PO_4, 20 mM $NaHCO_3$, 11.1 mM D-Glucose in deionized water, pH=7.35±0.05). The aorta was cannulated and the coronary system flushed with ice-cold Tyrode solution to reduce metabolic rate. The cannulated heart was then transferred to the experimental setup.

8.5.2 Experimental setup

Our experimental setup can be divided into the life support system and the optical mapping setup.

8.5.2.1 Life support system

Our life support system keeps the heart alive outside the body for up to 12 hours. It has a chamber that contains the Langendorff-perfused heart; the heart is also super-perfused with Tyrode solution so as to maintain ambient temperature at 37+/-1 degree Celsius. The Tyrode solution is aerated with 95% O_2. Since the oxygen concentration affects the pH, which needs to be maintained in a narrow range of 7.35 to 7.45. The pH and temperature stabilized solution is then pumped at a rate to maintain a pressure of 50 to 60 mmHg in the heart. We also use an excitation-contraction decoupler, either 2, 3-butanedione monoxime (BDM) or blebbistatin, to remove any motion artifact.

8.5.2.2 Optical Mapping System

The optical mapping system (Figure 28) consists of laser, mirrors, diffusers, filters and a CCD camera. The type of the laser used for illuminating the heart depends on the dye that is used for the experiment and in this project we plan to use voltage sensitive dye called Di-4-ANBDBQBS. DI-4-ANBDQBS stock solution was made by dissolving 10 mg of dye in 1.2 ml of pure ethanol, made fresh for each experiment. 30 μL of the stock DI-4-ANBDQBS solution was diluted with 15 mL of Tyrode's solution and injected as a bolus. Since Di-4-ANBDBQBS has an excitation wavelength of 671 nm, we use a red laser to illuminate the heart. A 1000 mW, 671 nm diode laser (Shanghai Dream Lasers) was

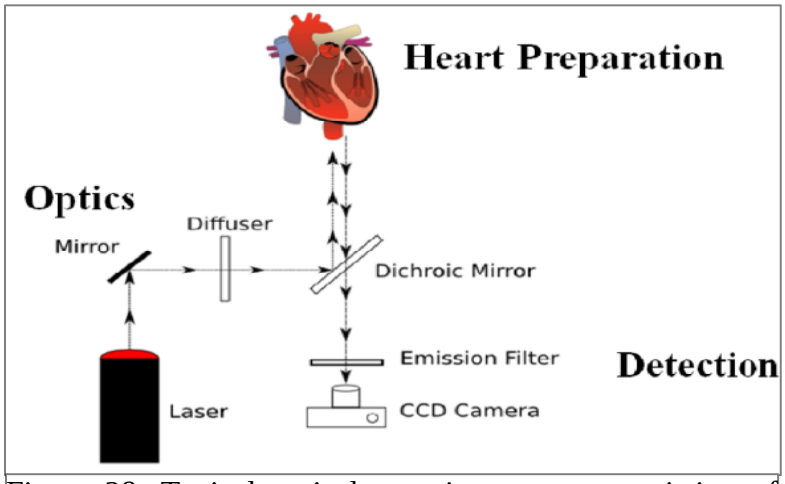

Figure 28: Typical optical mapping system consisting of heart preparation, optics and detection.

directed through a 5-degree conical diffusor and then through a dichroic mirror λ_{crit} = 690 nm) onto the heart to achieve uniform illumination.

8.6 Millisecond pacing of heart

The heart is stimulated with millisecond pulses at different points on the viable myocardium far from the ligation, very close to the ligation and in between the ligated tissue and the normal tissue and movies are recorded.

When the heart was excised at the end of 8 weeks, it was typically observed that the heart adhered to the ribcage at the apex. This is a normal phenomenon observed in coronary artery ligation surgery. The adhering tissue was carefully removed, while making sure that there is no damage to the myocardium. While complete removal was generally not possible, we pierced the tissue whenever we stimulated the heart from the apex.

8.7 Histology

At the end of optical mapping, the heart is perfused with TTC (2,3,5-triphenyl tetrazolium chloride) solution, 1 gm TTC dissolved in 100 ml of non-buffered saline. Infarct size can be assessed by using the staining agent TTC[75]. TTC stains the viable tissue to red while the infarcted tissue remains unstained[76]. This solution is recirculated for 30 to 40 minutes and then fixed in 10% neutral buffered formalin for further histological analysis.

CHAPTER 9

RESULTS AND DISCUSSION: TA-TREATED RAT HEARTS

9.1 Surgery performance

The objective of cohort I study was to develop infarct model to the point that we are confident that our surgical procedures are appropriate. In the first set of surgeries in cohort 1, 9 animal surgeries were performed and only 1 rat survived. One of the major difficulties that we faced during this study was the intubation. The vocal cleft in rats is very small, and the intubation catheter easily slips into the adjacent esophagus. Repeated unsuccessful attempts led to complications, such as laryngospasm glottic and local tissue trauma. Also, if the rat was not successfully intubated in the first few attempts, the animal would regain glottic reflexes, which made subsequent intubation attempts even more difficult. We tried intubation after tracheotomy, but even this more invasive approach yielded only modest improvements and probably reduced the chances for long-term survival. Another major difficulty was locating the LAD branch to ligate. A small opening to access the heart, about 2-3 of centimeters, and the motion of the heart while contracting add more difficulty in locating the branch of the LAD.

Placing an IV catheter to administer drugs was also difficult. Even the jugular vein (one of the biggest available veins) took several attempts and substantial time to cannulate, and in several animals it was not achieved and periodic interperitonal injection was used instead.

Only 1 out of the first 9 rats survived the surgery, and that survivor also died soon after the surgery. Overall, our procedure became lengthy, required improvisation, and had a low success rate.

Following the visit to Dr. Salloum's lab and the improvements in the surgery as described in the methods section, the surgery success rate in the cohort II study increased from 10% to 50%. The entire infarction surgery took only about 3-5 minutes, as opposed to the 1-2 hours previously. The surgery success rate in cohort III further increased to 70%.

9.2 Cohort III rat study

The objective of cohort III study was to collect preliminary data showing the efficacy of TA treated heart. In the cohort III study, we performed 14 surgeries, and 10 rats survived the surgery. From these 10 rats, 8 (4 control and 4 TA treated) survived for full 8 weeks while 1 was euthanized after 2 week and one after 4 weeks.

9.3 Control heart echocardiogram data

Reduced ejection fraction is one of the important parameters that causes mortality for those with myocardial infarction[77] . Also in case of animal models, it has been widely accepted that myocardial infarction in rats hearts decreases the ejection fraction[78] as is the case in heart failures in humans[79]. Another parameter that is widely seen in scientific publications related to infarct heart studies is the heart rate[80].

Decreased EF and increased heart rate are commonly used indicators for the presence of myocardial infarction. By evaluating these 2 parameters, we can determine the cardiac function and in turn determine the presence or absence of infarction.

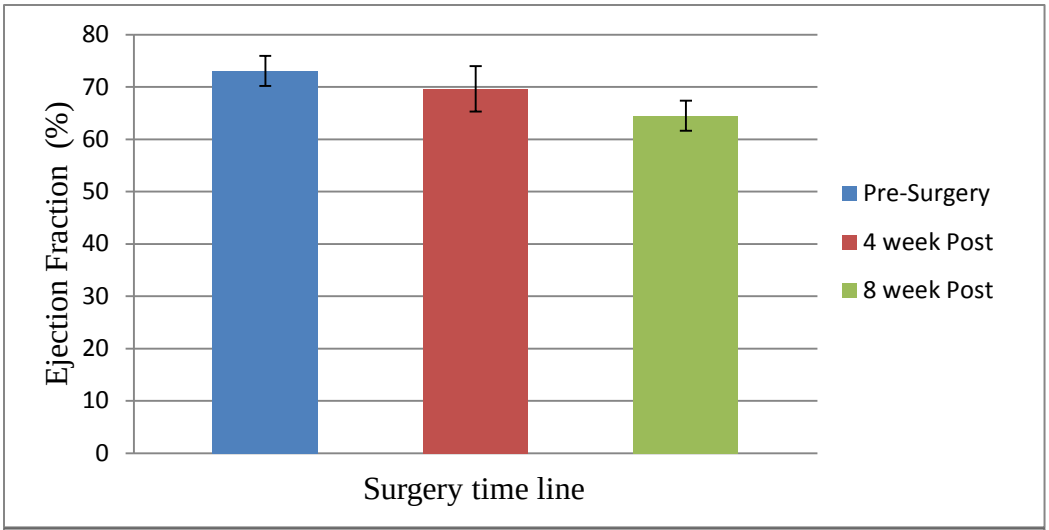

Figure 29: Ejection fraction in control hearts at pre-surgery, post-surgery 4weeks, and post-surgery 8 weeks.

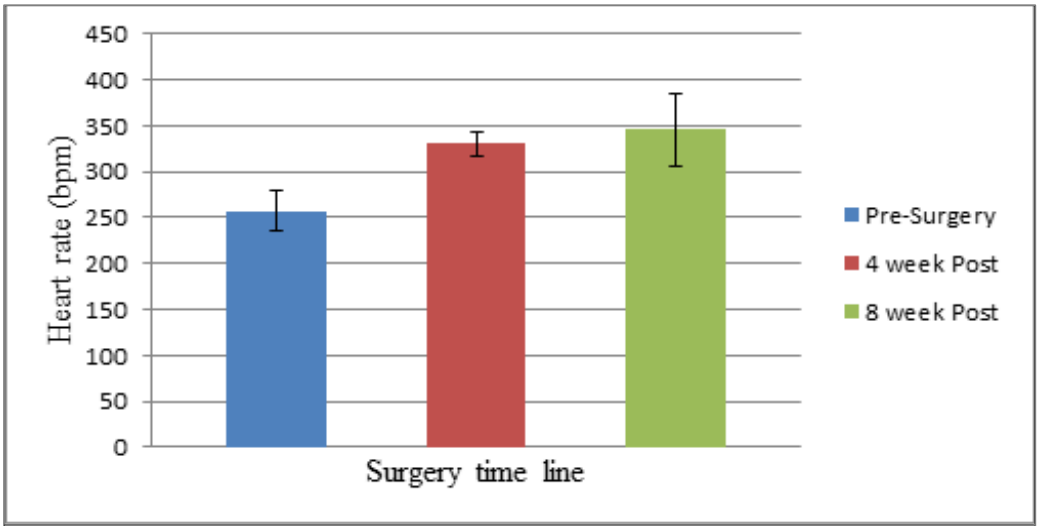

Figure 30: Heart rate in control hearts at pre-surgery, post-surgery 4weeks, and post-surgery 8 weeks

The typical ejection fraction in rats is about 72% to 75% while the typical range of heart rate in a normal rat is about 250 bpm. As the myocardial infarction progresses, the ability of the heart to contract decreases, thus reducing the ejection fraction. As the ejection fraction decreases, the heart tries to keep the same amount of blood being pumped out of the heart by increasing the heart rate. In cohort II, we performed myocardial infarction surgeries on 6 rats for the control group and all 6 survived the surgery, however, one died

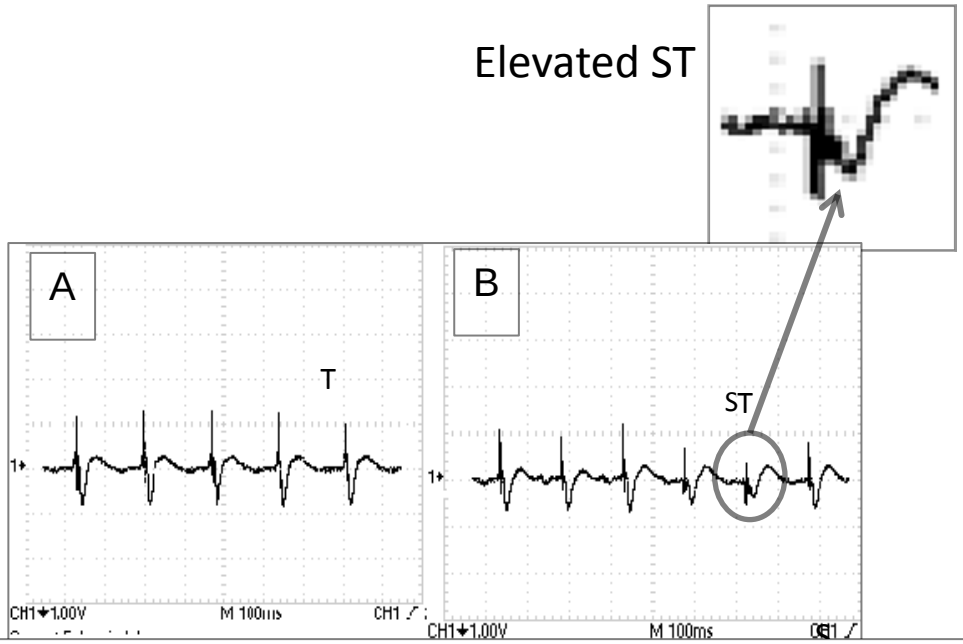

Figure 31: ECG recording in a control heart. Panel A shows the ECG just before ligating one of the branches of the LAD. The QRS complex looks regular and the heart rate is about 300 bpm. In Panel B at the end of 30 minutes of ligation. The QRS complex is irregular and the heart rate has increased to almost 480 bpm.

2 weeks after the surgery and second one died 4 weeks after the surgery.

The ejection fraction decreased in all the rats (see Figure 29) while heart rate increased as shown in Figure 30. The average ejection fraction pre-surgery was 73.1 % (SD: 3.31%) which dropped to 69.6% (SD: 5.02%, $p < 0.3$) after 4 weeks of surgery. At the end of 8 weeks the ejection fraction was 64.5% (SD: 3.32%,). The average drop in ejection fraction in control heart was 8% ($p < 0.05$), at the end of 8 weeks. In case of heart rate (Figure 30), the average pre-surgery heart rate in control rats was 257 bpm (SD: 25.4 bpm) which increased 330 bpm (SD: 12.6 bpm, $p < 0.05$) at the end of 4 weeks. At the end of 8 weeks the average heart rate rose up-to 345 bpm (45 bpm,). Thus the change in heart from a pre-surgery stage to 8 week post-surgery was 30% (88 bpm $p < 0.05$).

During the process of surgery, we monitored the electrocardiogram to assess the condition of the heart in terms heart rate and shape of the QRS. Figure 31 shows a representative picture of an ECG recording during the surgery. Figure 31A shows the ECG recording in a control heart just before the ligation and Figure 31B, shows the ECG recording at the end of 30 minutes of infarction in the same heart. The rat in study had an initial 300 bpm heart rate at the start of the surgery, which increased to 500 bpm at the end of the surgery. This animal died at the end of the surgery. Also the QRS complex have approximate 50 % decrease in amplitude while the heart rate increased by 60%, (see Figure 31B). This change in QRS complex amplitude was observed in all hearts however the variation in the amplitude changed from heart to heart. Also, the ST segment of the ECG shows elevation compared to pre-ligation recording. The elevated ST segment suggests the presence of myocardial ischemia which could soon result in severe

infarction[81], however, the animal in this study did not survive the surgery. The ECG recordings were not used for quantitative analysis.

9.4 Electrical activity in control hearts

To determine which part of the cardiac surface has impaired electrical activity, we stimulated the tissue at multiple locations around the ligation and monitored the response of the heart using optical mapping. Figure 32 shows a representative figure of the electrical activity in control hearts. In Figure 32A, the stimulation site and the ligation site are marked by black dot and a circle respectively. Figure 32B shows the activation

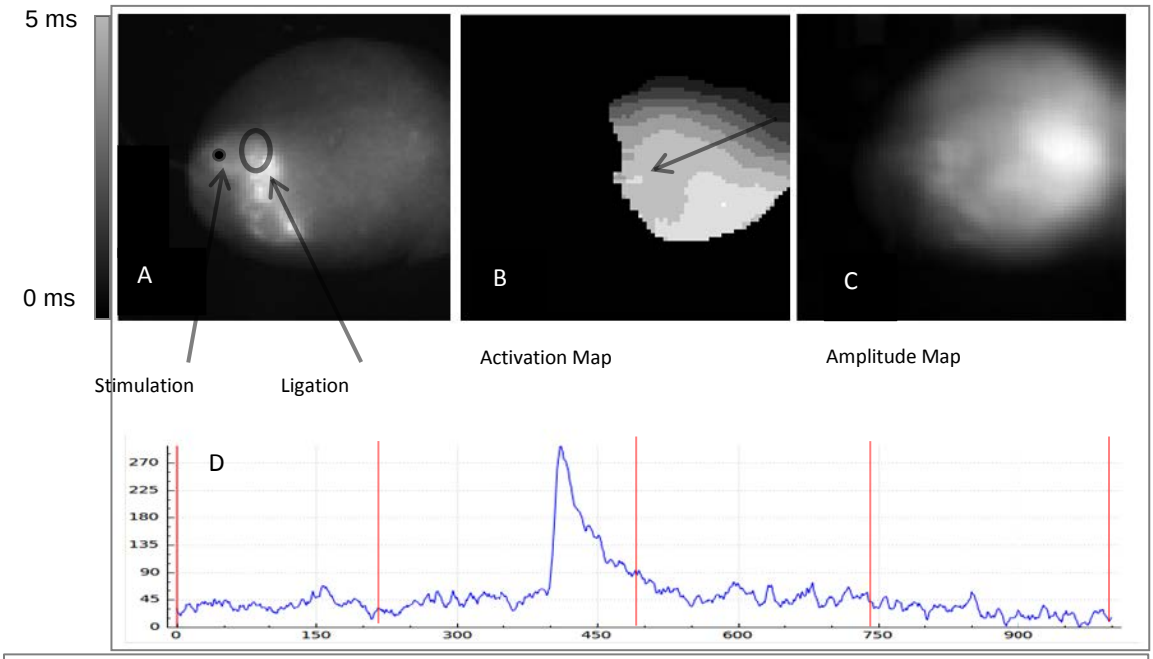

Figure 32: Optical mapping of control heart. Panel A shows the fluorescence image of control heart. Panel B is the amplitude map of Panel A. Panel C shows the activation map in the same heart, when the heart is stimulated in the infarct zone. Panel D shows the action potential recording from the same heart.

map, where the darker shades represent the earliest activation times. Figure 32C shows the amplitude map of the heart. The heart was stimulated from close to the ligation at a frequency of 3 Hz, however, the action potential recording shows the presence of one activation. This activation according to the activation map starts from the base of the heart suggesting sinus rhythm. The heart failed to respond to the ms stimulation when it was paced close to the ligated region, giving a strong evidence for the presence of infarction.

9.5 TA treated heart echocardiogram data

As discussed in Section 7.3, the ejection fraction and heart rate are used to assess the efficacy of TA in reducing the severity of the infarct. If TA actually regenerates the infarcted heart tissue, then the ejection fraction and heart rate should be closer to normal heart echocardiogram than the ejection fraction of control hearts. The 4-week and 8-week echo-cardiogram data would reveal the effectiveness of TA. In the TA-treated

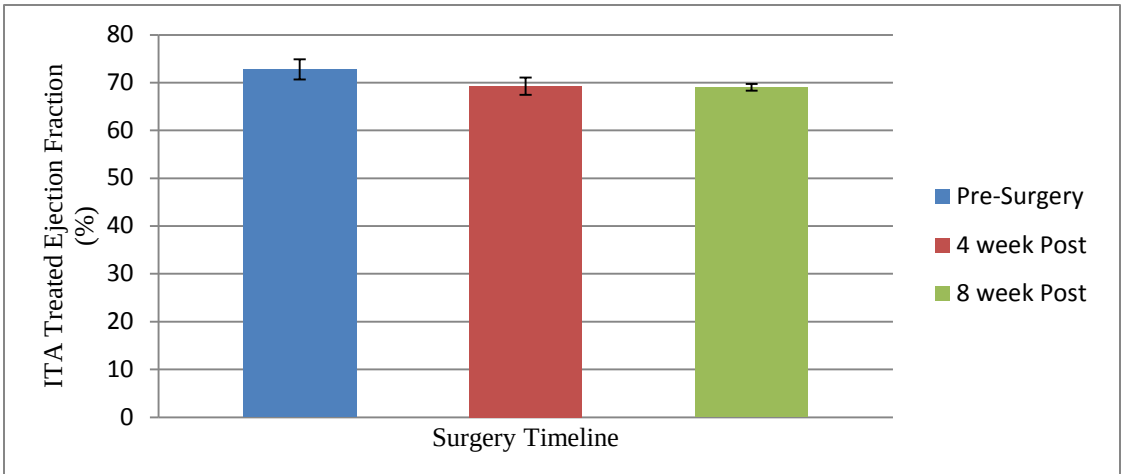

Figure 33: Ejection fraction in TA-treated hearts at pre-surgery, post-surgery 4weeks, and post-surgery 8 weeks

hearts, the average ejection fraction (Figure 33) at pre-surgery was 72.8% (SD:2.4%) which decreased by less than 2% ($p < 0.07$) to 69.65 % (SD: 1.78%) and remained so until 8 weeks.

In the TA-treated hearts, the average pre-surgery heart rate (Figure 34) was 262 bpm (SD:20 bpm) which increased to 314 bpm ($p < 0.05$) at the end of 4 weeks and then slightly increased to 323 bpm (SD: 21 bpm) at the end of 8 weeks.

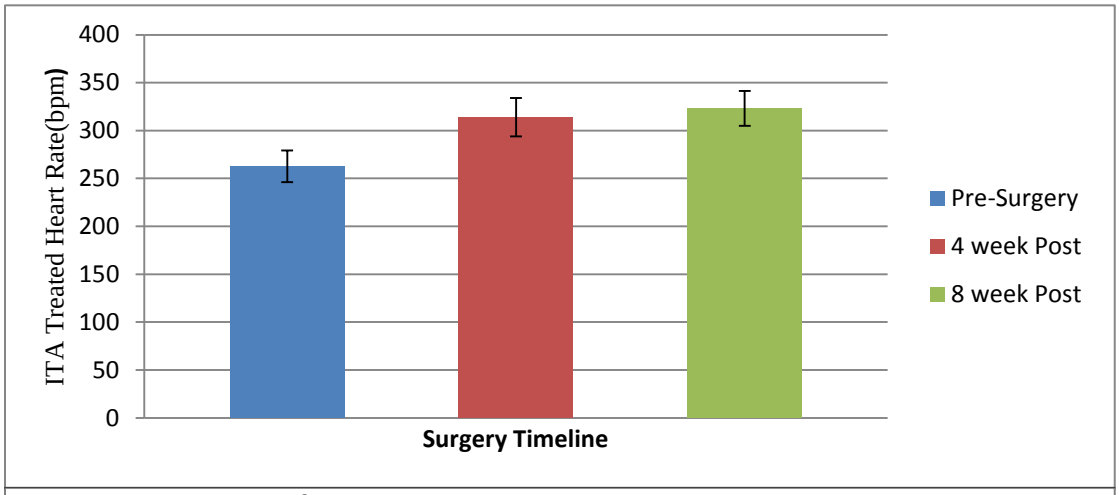

Figure 34: Heart rate of TA treated hearts at pre-surgery, post-surgery 4weeks and post-surgery 8 weeks

9.6 Comparison of control and TA-treated hearts

In control hearts the ejection fraction dropped from the pre-surgery to 4 weeks to 8weeks while the heart rate increased as the time passed from pre-surgery to 8weeks. In the TA treated hearts, the ejection fraction decreased initially from pre-surgery to 4 weeks but

after that it remained the same while the heart rate also increased during the first 4 weeks after which it stabilized.

The average drop in the ejection fraction in TA treated heart was about 3% compared to 9.5 % ($p < 0.02$) in control hearts. Also the heart rate in control heart at end of 8 week was 346 bpm (SD 45 bpm), a change of 35% where as in TA treated heart, the average heart rate was 323 bpm (SD: 21 bpm,), a change of 25 % ($p < 0.4$). These data also suggest that TA may substantially reduce infarct development, but experiments with larger cohorts are needed to validate this finding.

9.7 Improved electrical activity in TA injected hearts

Optical mapping revealed that the surviving tissue in TA treated hearts had normal electrical activity, in particularly no slowing of conduction or changes in action potential duration relative to normal healthy control hearts. Figure 35A shows a photograph of a rat heart in our optical mapping setup. Figure 35B shows a representative activation map for a saline-treated heart with a large infarct. The smooth transition from black to white, with approximately equal widths for the different shades of gray, indicates that the propagation velocity of excitation is approximately constant.

A rough estimate of the propagation velocity can be obtained by dividing the distance between the stimulation site and the point of latest activation (~12 mm) by the time of the latest activation (25 mm); this approximation yields a propagation speed of ~ 50 cm/s,

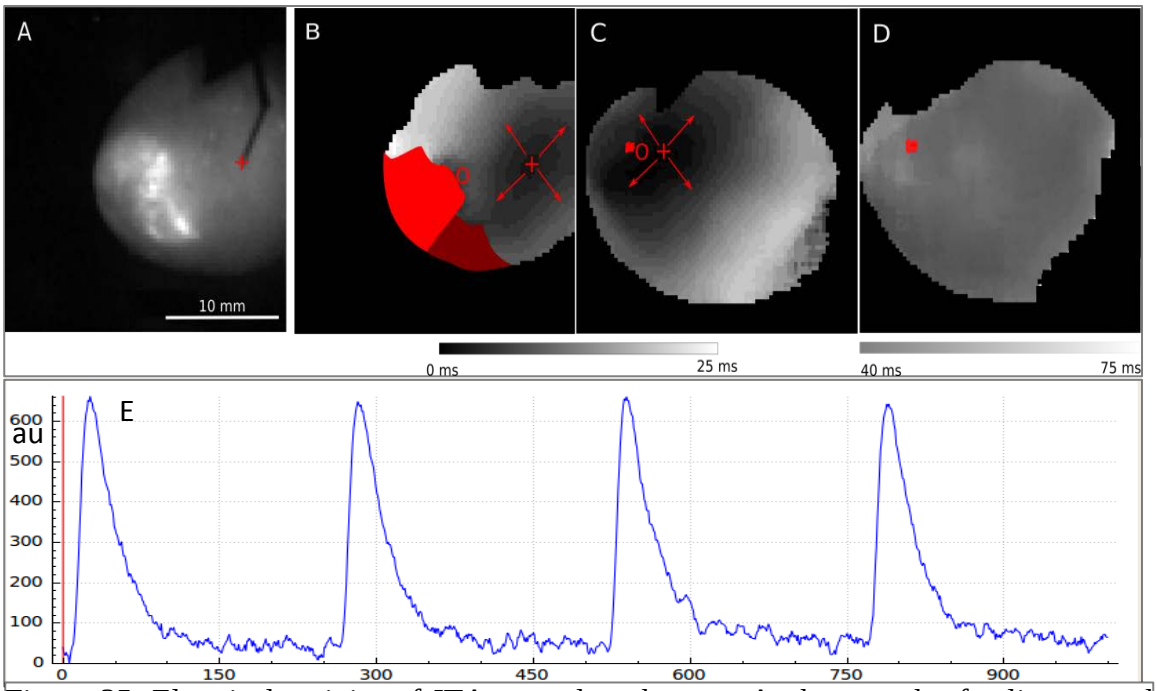

Figure 35. Electrical activity of ITA-treated rat hearts. A photograph of saline-treated heart is shown in the optical mapping setup for reference (A). The stimulation electrode can be seen as a black line, a red "+" has been placed at its tip to mark the stimulation site. The bright areas in the left part of the heart are reflections from a thin layer of pericardium that attached to the epicardium. Representative activation map of saline-treated heart are shown in (B) (from the same heart as in Panel A). Arrows indicate the direction in which activation propagates from stimulation site. Red circle marks the ligation site; bright red area the infarct, dark red is not infarcted by the attached pericardium precluded computation of activation time. Representative activation map of ITA-treated heart are shown in (C), details as in Panel (B). Representative action potential duration map of ITA-treated heart are further shown (D). Panel E shows the action potential recording in the ITA treated region

typical for ventricular myocardial tissue. Figure 34C shows a representative activation map for TA-treated heart with a small infarct. The propagation of excitation is smooth with a propagation speed close to that of saline-treated hearts. Note in particular that there is no propagation block or slowing of conduction in the vicinity of the infarct; both would be visible in an activation map as more abrupt transitions from dark to light. Figure 35D shows the distribution of action potential durations (APDs) in an TA-treated heart (same heart as in Panel B). The APDs are highly uniform across the ventricle, and in particular, there is no change in APD around the infarct, another sign that the area around the infarct exhibits normal electrical activity. All TA-treated (n=4) hearts tested exhibited activation maps and action potential maps consistent with the representative examples shown here, with no sign of impeded conduction or change in APD around the infarcts.

9.8 TA remains at the site of injection

An important question is whether TA that we injected remains at the injection site or flows back out of the tissue once the needle is remove or would flow back due to the muscle resistance. This was important to know because, the whole study was hypothesized on the basis that TA remains at the site of inject and plays the major role recruiting the cardiac stem cells and promoting angiogenesis at that site of injury. We confirmed that the TA remains at the injection site, but because of an NDA, we are not able to provide the details here.

9.9 Staining

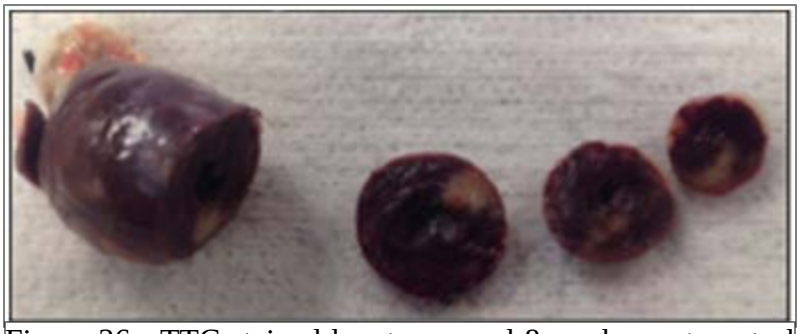

Figure 36: TTC stained heart assessed 8 weeks post control hearts, removed, fixed and sectioned.

In Figure 36, we show a control heart that was stained with TTC, The white areas on the sections are the area that remained unstained due to myocardial infarction.

9.10 Discussion

Studies have shown that the ejection fraction decreases while heart rate increase as soon as after the onset of the myocardial infarction symptoms[82], [83]. These echocardiograms measurements suggests that the presence of an infarct[81] in this heart**.** The echocardiogram data also show that TA is deliverable to the myocardium where it safely and significantly improves ejection fraction in rats with a moderately sized infarction, accomplished without creating electrically compromised tissue.

Optical mapping experiments show that TA not only increases the amount of surviving tissue, but that this tissue is also fully functional from an electrophysiological point of

view. This finding is important, because insufficiently regenerated tissue could lead to slow conduction, changes in action potential duration, and unidirectional block, which could together provide a substrate for arrhythmias that could be even worse than a larger infarct. This is a notable concern as other approaches to regenerating myocardial tissue have reported aberrant electrical activity in the heart, including recent use of embryonic stem cell (ESC)-derived cardiomyocytes applied to a primate heart[84]. Since no electrophysiological abnormalities were seen in any of the TA injected hearts, it is concluded that the reduction of infarct size that TA provides does not come at the cost of arrhythmia risks.

9.11 Conclusion

With continued successful preclinical development, this work may lead to a potential therapeutic agent for myocardial infarction. TA has advantage because of its human tissue origin and has potential for delivery using minimal invasive surgery. Also, TA could reduce the immense pressures for organ transplantation and the use of external assist devices, both with their associated risky surgical procedures, and thus savings lives and restoring health with this regenerative medicine approach.

CHAPTER 10

CONCLUSIONS AND FUTURE WORK

In Chapter I, we showed that the geodesic, which predicts the shape of stationary filaments of scroll waves, is valid even for large filament curvatures and for abrupt changes in diffusivity, as long as these changes occur far enough from the filament. Our finding greatly enhances the utility of the geodesic principle, and therefore contributes to the understanding of the mechanisms underlying ventricular fibrillation.

The treatment of ventricular fibrillation was the subject of Chapters 2 - 5, in which we showed how nanosecond pulsed electric fields (nsPEFs) can be used to stimulate and defibrillate rabbit hearts. The nsPEF amplitude required to stimulate rabbit hearts lies in the range of 0.75 to 1 kV over a distance of 3 cm, while defibrillation required an amplitude of 2.3-2.4 kV over 3 cm. This means that the energy required to defibrillate the rabbit heart with nsPEFs is eight times lower than the corresponding energy for millisecond defibrillation, which is a dramatic improvement.

NsPEF application did not significantly affect the electrical activity of the heart: The action potential duration was unchanged, while the diastolic interval was affected, but only for a single beat after the nsPEF application. Histological stains did not reveal any damage in the vicinity of the electrodes in a heart that had been exposed to a large number of shocks.

Our future plans are to study the efficacy of nsPEF defibrillation for a variety of shock parameters and at the same time study the potential damage that nsPEFs may do in more detail. Then we will move to a large animal model (pigs) to prepare a clinical trial and move nsPEF defibrillation to the clinical practice.

In Chapters 5 – 7, we developed a rat model of myocardial infarction and, using this model, showed that an injectable therapeutic agent is effective in limiting the infarct size resulting from ligation of a coronary artery. Successful creation of infarction was verified by echocardiography (using ejection fraction and heart rate).

Injection of the therapeutic agent (TA) significantly reduced the drop in ejection fraction, a sign that the developed infarct was smaller. The rise in heart rate associated with infarction was also reduced, although larger animal numbers will be necessary to establish significance of this result. Optical mapping experiments showed no sign of arrhythmias in the vicinity of the infarction.

To take TA as a treatment alternative for myocardial infarction to clinical levels will require studies on toxicity. Once the safety of TA has been proven in rats, we will study the efficacy of TA in large animals (pigs).

In summary, this thesis presents new approaches to understanding cardiac arrhythmias, treating cardiac arrhythmias, and treating myocardial infarction. Our approaches have

identified specific treatments that after further testing may become approved for clinical use, and may make a lasting contribution to treating cardiac disease.

REFERENCES

[1] D. Dormann, B. Vasiev, and C. J. Weijer, “Becoming Multicellular by Aggregation; The Morphogenesis of the Social Amoebae Dicyostelium discoideum,” *J. Biol. Phys.*, vol. 28, no. 4, pp. 765–780, Dec. 2002.

[2] J. Keener, “Waves in Excitable Media,” *SIAM J. Appl. Math.*, vol. 39, no. 3, pp. 528–548, Dec. 1980.

[3] A. V. Holden, A. P. Benson, and G. Halley, “Cardiac arrhythmias: dynamics and geometry,” *PAMM*, vol. 7, no. 1, pp. 1041703–1041704, Dec. 2007.

[4] B. Ballarò, P. G. Reas, and R. Riccardi, “Mathematical models for excitable systems in biology and medicine,” *Riv. Biol.*, vol. 100, no. 2, pp. 247–266, Aug. 2007.

[5] B. M. Sager, “Propagation of traveling waves in excitable media.,” *Genes Dev.*, vol. 10, no. 18, pp. 2237–2250, Sep. 1996.

[6] A. T. Winfree, “Scroll-Shaped Waves of Chemical Activity in Three Dimensions,” *Science*, vol. 181, no. 4103, pp. 937–939, Sep. 1973.

[7] F. Siegert and C. J. Weijer, “Three-dimensional scroll waves organize Dictyostelium slugs,” *Proc. Natl. Acad. Sci.*, vol. 89, no. 14, pp. 6433–6437, Jul. 1992.

[8] B. J. Welsh, J. Gomatam, and A. E. Burgess, “Three-dimensional chemical waves in the Belousov–Zhabotinskii reaction,” *Nature*, vol. 304, no. 5927, pp. 611–614, Aug. 1983.

[9] T. B. Jr and O. Steinbock, “Three-dimensional spiral waves in an excitable reaction system: Initiation and dynamics of scroll rings and scroll ring pairs,” *Chaos Interdiscip. J. Nonlinear Sci.*, vol. 18, no. 2, p. 026102, Jun. 2008.

[10] S. Alonso, F. Sagués, and A. S. Mikhailov, “Taming Winfree Turbulence of Scroll Waves in Excitable Media,” *Science*, vol. 299, no. 5613, pp. 1722–1725, Mar. 2003.

[11] I. R. Efimov, V. Sidorov, Y. Cheng, and B. Wollenzier, “Evidence of Three-Dimensional Scroll Waves with Ribbon-Shaped Filament as a Mechanism of Ventricular Tachycardia in the Isolated Rabbit Heart,” *J. Cardiovasc. Electrophysiol.*, vol. 10, no. 11, pp. 1452–1462, Nov. 1999.

[12] B. G. Mitrea, M. Wellner, and A. M. Pertsov, “Monitoring intramyocardial reentry using alternating transillumination,” in *Annual International Conference of the IEEE Engineering in Medicine and Biology Society, 2009. EMBC 2009*, 2009, pp. 4194–4197.

[13] W. T. Baxter, S. F. Mironov, A. V. Zaitsev, J. Jalife, and A. M. Pertsov, “Visualizing Excitation Waves inside Cardiac Muscle Using Transillumination,” *Biophys. J.*, vol. 80, no. 1, pp. 516–530, Jan. 2001.

[14] A. V. Panfilov, “Spiral breakup as a model of ventricular fibrillation,” *Chaos Interdiscip. J. Nonlinear Sci.*, vol. 8, no. 1, pp. 57–64, Mar. 1998.

[15] R. M. Zaritski, S. F. Mironov, and A. M. Pertsov, “Intermittent Self-Organization of Scroll Wave Turbulence in Three-Dimensional Excitable Media,” *Phys. Rev. Lett.*, vol. 92, no. 16, p. 168302, Apr. 2004.

[16] F. Fenton and A. Karma, “Fiber-Rotation-Induced Vortex Turbulence in Thick Myocardium,” *Phys. Rev. Lett.*, vol. 81, no. 2, pp. 481–484, Jul. 1998.

[17] M. Vinson, A. Pertsov, and J. Jalife, “Anchoring of vortex filaments in 3D excitable media,” *Phys. Nonlinear Phenom.*, vol. 72, no. 1, pp. 119–134, Apr. 1994.

[18] M. Wellner, C. Zemlin, and A. M. Pertsov, “Frustrated drift of an anchored scroll-wave filament and the geodesic principle,” *Phys. Rev. E*, vol. 82, no. 3, p. 036122, Sep. 2010.

[19] Z. A. Jiménez, B. Marts, and O. Steinbock, “Pinned Scroll Rings in an Excitable System,” *Phys. Rev. Lett.*, vol. 102, no. 24, p. 244101, Jun. 2009.

[20] J. Keener, “Waves in Excitable Media,” *SIAM J. Appl. Math.*, vol. 39, no. 3, pp. 528–548, Dec. 1980.

[21] C. S. Henriquez, “Simulating the electrical behavior of cardiac tissue using the bidomain model,” *Crit. Rev. Biomed. Eng.*, vol. 21, no. 1, pp. 1–77, 1993.

[22] M. J. Burgess, B. M. Steinhaus, K. W. Spitzer, and P. R. Ershler, “Nonuniform epicardial activation and repolarization properties of in vivo canine pulmonary conus.,” *Circ. Res.*, vol. 62, no. 2, pp. 233–246, Feb. 1988.

[23] G.-X. Yan, W. Shimizu, and C. Antzelevitch, “Characteristics and Distribution of M Cells in Arterially Perfused Canine Left Ventricular Wedge Preparations,” *Circulation*, vol. 98, no. 18, pp. 1921–1927, Nov. 1998.

[24] R. J. Kim, S. Iwai, S. M. Markowitz, B. K. Shah, K. M. Stein, and B. B. Lerman, “Clinical and Electrophysiological Spectrum of Idiopathic Ventricular Outflow Tract Arrhythmias,” *J. Am. Coll. Cardiol.*, vol. 49, no. 20, pp. 2035–2043, May 2007.

[25] V. N. Biktashev, A. V. Holden, and H. Zhang, “Tension of Organizing Filaments of Scroll Waves,” *Philos. Trans. R. Soc. Lond. Math. Phys. Eng. Sci.*, vol. 347, no. 1685, pp. 611–630, Jun. 1994.

[26] D. Barkley, “A model for fast computer simulation of waves in excitable media,” *Phys. Nonlinear Phenom.*, vol. 49, no. 1, pp. 61–70, Apr. 1991.

[27] O. A. Mornev, “Refraction of autowaves: Tangent rule,” *J. Exp. Theor. Phys. Lett.*, vol. 80, no. 12, pp. 721–724, Dec. 2004.

[28] I. V. Biktasheva, D. Barkley, V. N. Biktashev, and A. J. Foulkes, “Computation of the drift velocity of spiral waves using response functions,” *Phys. Rev. E*, vol. 81, no. 6, p. 066202, Jun. 2010.

[29] C. W. Zemlin and A. M. Pertsov, “Anchoring of Drifting Spiral and Scroll Waves to Impermeable Inclusions in Excitable Media,” *Phys. Rev. Lett.*, vol. 109, no. 3, p. 038303, Jul. 2012.

[30] K. H. W. J. ten Tusscher and A. V. Panfilov, “Eikonal Formulation of the Minimal Principle for Scroll Wave Filaments,” *Phys. Rev. Lett.*, vol. 93, no. 10, p. 108106, Sep. 2004.

[31] M. Wellner, O. Berenfeld, J. Jalife, and A. M. Pertsov, “Minimal principle for rotor filaments,” *Proc. Natl. Acad. Sci.*, vol. 99, no. 12, pp. 8015–8018, Jun. 2002.

[32] H. Verschelde, H. Dierckx, and O. Bernus, “Covariant Stringlike Dynamics of Scroll Wave Filaments in Anisotropic Cardiac Tissue,” *Phys. Rev. Lett.*, vol. 99, no. 16, p. 168104, Oct. 2007.

[33] R. J. Sung and M. R. Lauer, *Fundamental Approaches to the Management of Cardiac Arrhythmias*. Springer Science & Business Media, 2012.

[34] R. Veeraraghavan, R. G. Gourdie, and S. Poelzing, “Mechanisms of cardiac conduction: a history of revisions,” *Am. J. Physiol. - Heart Circ. Physiol.*, vol. 306, no. 5, pp. H619–H627, Mar. 2014.

[35] P. Jones and N. Lodé, “Ventricular fibrillation and defibrillation,” *Arch. Dis. Child.*, vol. 92, no. 10, pp. 916–921, Oct. 2007.

[36] G. H. Bardy, B. E. Gliner, P. J. Kudenchuk, J. E. Poole, G. L. Dolack, G. K. Jones, J. Anderson, C. Troutman, and G. Johnson, “Truncated biphasic pulses for transthoracic defibrillation,” *Circulation*, vol. 91, no. 6, pp. 1768–1774, Mar. 1995.

[37] J.-P. Didon, G. Fontaine, R. D. White, I. Jekova, J.-J. Schmid, and A. Cansell, “Clinical experience with a low-energy pulsed biphasic waveform in out-of-hospital cardiac arrest,” *Resuscitation*, vol. 76, no. 3, pp. 350–353, Mar. 2008.

[38] J. Tibballs, B. Carter, N. J. Kiraly, P. Ragg, and M. Clifford, “External and internal biphasic direct current shock doses for pediatric ventricular fibrillation and pulseless ventricular tachycardia,” *Pediatr. Crit. Care Med. J. Soc. Crit. Care Med. World Fed. Pediatr. Intensive Crit. Care Soc.*, vol. 12, no. 1, pp. 14–20, Jan. 2011.

[39] W. G. and P. of E. Reviewers, R. O. Cummins, M. F. Hazinski, R. E. Kerber, P. Kudenchuk, L. Becker, G. Nichol, B. Malanga, T. P. Aufderheide, E. M. Stapleton, K. Kern, J. P. Ornato, A. Sanders, T. Valenzuela, and M. Eisenberg, “Low-Energy Biphasic Waveform Defibrillation: Evidence-Based Review Applied to Emergency Cardiovascular Care Guidelines A Statement for Healthcare Professionals From the American Heart Association Committee on Emergency Cardiovascular Care and the Subcommittees on Basic Life Support, Advanced Cardiac Life Support, and Pediatric Resuscitation,” *Circulation*, vol. 97, no. 16, pp. 1654–1667, Apr. 1998.

[40] A. R. J. Mitchell, P. a. R. Spurrell, K. Kamalvand, M. Higson, R. Shanmuganathan, N. R. Patel, and N. Sulke, “What is the optimal electrode configuration for atrial defibrillators in man?,” *Eur. Eur. Pacing Arrhythm. Card. Electrophysiol. J. Work.*

Groups Card. Pacing Arrhythm. Card. Cell. Electrophysiol. Eur. Soc. Cardiol., vol. 4, no. 1, pp. 41–44, Jan. 2002.

[41] P. R. Martens, J. K. Russell, B. Wolcke, H. Paschen, M. Kuisma, B. E. Gliner, W. D. Weaver, L. Bossaert, D. Chamberlain, and T. Schneider, "Optimal Response to Cardiac Arrest study: defibrillation waveform effects," *Resuscitation*, vol. 49, no. 3, pp. 233–243, Jun. 2001.

[42] S. Behrens, C. Li, P. Kirchhof, F. L. Fabritz, and M. R. Franz, "Reduced arrhythmogenicity of biphasic versus monophasic T-wave shocks. Implications for defibrillation efficacy," *Circulation*, vol. 94, no. 8, pp. 1974–1980, Oct. 1996.

[43] G. Ristagno, T. Yu, W. Quan, G. Freeman, and Y. Li, "Current is better than energy as predictor of success for biphasic defibrillatory shocks in a porcine model of ventricular fibrillation," *Resuscitation*, vol. 84, no. 5, pp. 678–683, May 2013.

[44] G. H. Bardy, F. E. Marchlinski, A. D. Sharma, S. J. Worley, R. M. Luceri, R. Yee, B. D. Halperin, C. L. Fellows, T. S. Ahern, D. A. Chilson, D. L. Packer, D. J. Wilber, T. A. Mattioni, R. Reddy, R. A. Kronmal, and R. Lazzara, "Multicenter comparison of truncated biphasic shocks and standard damped sine wave monophasic shocks for transthoracic ventricular defibrillation. Transthoracic Investigators," *Circulation*, vol. 94, no. 10, pp. 2507–2514, Nov. 1996.

[45] S. Tanabe, H. Yasunaga, T. Ogawa, S. Koike, M. Akahane, H. Horiguchi, T. Hatanaka, H. Yokota, and T. Imamura, "Comparison of outcomes after use of biphasic or monophasic defibrillators among out-of-hospital cardiac arrest patients: a nationwide population-based observational study," *Circ. Cardiovasc. Qual. Outcomes*, vol. 5, no. 5, pp. 689–696, Sep. 2012.

[46] C.-H. Wang, C.-H. Huang, W.-T. Chang, M.-S. Tsai, S. S.-H. Liu, C.-Y. Wu, Y.-C. Lee, Z.-S. Yen, C.-C. Fang, and W.-J. Chen, "Biphasic versus monophasic defibrillation in out-of-hospital cardiac arrest: a systematic review and meta-analysis," *Am. J. Emerg. Med.*, vol. 31, no. 10, pp. 1472–1478, Oct. 2013.

[47] G. P. Tolstykh, G. L. T. Thompson, H. T. Beier, C. C. Roth, and B. L. Ibey, "Nanosecond pulsed electric fields activate intracellular signaling pathways," *SPIE Newsroom*, Mar. 2013.

[48] S. J. Beebe and K. H. Schoenbach, "Nanosecond pulsed electric fields: a new stimulus to activate intracellular signaling," *J. Biomed. Biotechnol.*, vol. 2005, no. 4, pp. 297–300, 2005.

[49] W. Ren and S. J. Beebe, "An apoptosis targeted stimulus with nanosecond pulsed electric fields (nsPEFs) in E4 squamous cell carcinoma," *Apoptosis Int. J. Program. Cell Death*, vol. 16, no. 4, pp. 382–393, Apr. 2011.

[50] M. Nagahama, N. Shimomura, A. Nakagawa, K. Teranishi, Y. Uto, and H. Hori, "In vivo experimental study of nanosecond pulsed electric field effects on solid tumors," *IEEE Trans. Dielectr. Electr. Insul.*, vol. 20, no. 4, pp. 1266–1272, Aug. 2013.

[51] K. H. Schoenbach, B. Hargrave, R. P. Joshi, J. F. Kolb, R. Nuccitelli, C. Osgood, A. Pakhomov, M. Stacey, R. J. Swanson, J. A. White, S. Xiao, J. Zhang, S. J. Beebe, P. F. Blackmore, and E. S. Buescher, "Bioelectric Effects of Intense Nanosecond Pulses," *IEEE Trans. Dielectr. Electr. Insul.*, vol. 14, no. 5, pp. 1088–1109, 2007.

[52] T. R. Gowrishankar and J. C. Weaver, “Electrical behavior and pore accumulation in a multicellular model for conventional and supra-electroporation,” *Biochem. Biophys. Res. Commun.*, vol. 349, no. 2, pp. 643–653, Oct. 2006.

[53] C. C. Roth, G. P. Tolstykh, J. A. Payne, M. A. Kuipers, G. L. Thompson, M. N. DeSilva, and B. L. Ibey, “Nanosecond pulsed electric field thresholds for nanopore formation in neural cells,” *J. Biomed. Opt.*, vol. 18, no. 3, p. 035005, Mar. 2013.

[54] W. R. Rogers, J. H. Merritt, J. J.A. Comeaux, C. T. Kuhnel, D. F. Moreland, D. G. Teltschik, J. H. Lucas, and M. R. Murphy, “Strength-duration curve for an electrically excitable tissue extended down to near 1 nanosecond,” *IEEE Trans. Plasma Sci.*, vol. 32, no. 4, pp. 1587–1599, Aug. 2004.

[55] P. Weismüller, P. Richter, L. Binner, G. Grossmann, W. Hemmer, M. Höher, M. Kochs, and V. Hombach, “Direct current application: easy induction of ventricular fibrillation for the determination of the defibrillation threshold in patients with implantable cardioverter defibrillators,” *Pacing Clin. Electrophysiol. PACE*, vol. 15, no. 8, pp. 1137–1143, Aug. 1992.

[56] M. Ogawa, N. Morita, L. Tang, H. S. Karagueuzian, J. N. Weiss, S.-F. Lin, and P.-S. Chen, “Mechanisms of Recurrent Ventricular Fibrillation in a Rabbit Model of Pacing-Induced Heart Failure,” *Heart Rhythm Off. J. Heart Rhythm Soc.*, vol. 6, no. 6, pp. 784–792, Jun. 2009.

[57] I. Kodama, I. Sakuma, N. Shibata, S. B. Knisley, R. Niwa, and H. Honjo, “Regional differences in arrhythmogenic aftereffects of high intensity DC stimulation in the ventricles,” *Pacing Clin. Electrophysiol. PACE*, vol. 23, no. 5, pp. 807–817, May 2000.

[58] B. Sowell and V. G. Fast, “Ionic mechanism of shock-induced arrhythmias: role of intracellular calcium,” *Heart Rhythm Off. J. Heart Rhythm Soc.*, vol. 9, no. 1, pp. 96–104, Jan. 2012.

[59] A. M. Russo and M. K. Chung, “Is defibrillation testing necessary?,” *Cardiol. Clin.*, vol. 32, no. 2, pp. 211–224, May 2014.

[60] E. R. Uyguanco, A. Berger, A. S. Budzikowski, M. Gunsburg, and J. Kassotis, “Management of high defibrillation threshold,” *Expert Rev. Cardiovasc. Ther.*, vol. 6, no. 9, pp. 1237–1248, Oct. 2008.

[61] D. Mozaffarian, E. J. Benjamin, A. S. Go, D. K. Arnett, M. J. Blaha, M. Cushman, S. de Ferranti, J.-P. Després, H. J. Fullerton, V. J. Howard, M. D. Huffman, S. E. Judd, B. M. Kissela, D. T. Lackland, J. H. Lichtman, L. D. Lisabeth, S. Liu, R. H. Mackey, D. B. Matchar, D. K. McGuire, E. R. Mohler, C. S. Moy, P. Muntner, M. E. Mussolino, K. Nasir, R. W. Neumar, G. Nichol, L. Palaniappan, D. K. Pandey, M. J. Reeves, C. J. Rodriguez, P. D. Sorlie, J. Stein, A. Towfighi, T. N. Turan, S. S. Virani, J. Z. Willey, D. Woo, R. W. Yeh, M. B. Turner, and American Heart Association Statistics Committee and Stroke Statistics Subcommittee, “Heart disease and stroke statistics--2015 update: a report from the American Heart Association,” *Circulation*, vol. 131, no. 4, pp. e29–322, Jan. 2015.

[62] A. Ahmadi, J. Leipsic, R. Blankstein, C. Taylor, H. Hecht, G. W. Stone, and J. Narula, “Do Plaques Rapidly Progress Prior to Myocardial Infarction? The Interplay Between Plaque Vulnerability and Progression,” *Circ. Res.*, vol. 117, no. 1, pp. 99–104, Jun. 2015.

[63] J F Moran and R. M. Gunnar, “Pathophysiology of Heart Block,” *Annu. Rev. Med.*, vol. 26, no. 1, pp. 471–483, 1975.

[64] D. L. Mann, “Mechanisms and models in heart failure: A combinatorial approach,” *Circulation*, vol. 100, no. 9, pp. 999–1008, Aug. 1999.

[65] D. L. Mann, R. Bogaev, and G. D. Buckberg, “Cardiac remodelling and myocardial recovery: lost in translation?,” *Eur. J. Heart Fail.*, vol. 12, no. 8, pp. 789–796, Aug. 2010.

[66] M. G. S. J. Sutton and N. Sharpe, “Left Ventricular Remodeling After Myocardial Infarction Pathophysiology and Therapy,” *Circulation*, vol. 101, no. 25, pp. 2981–2988, Jun. 2000.

[67] “Stem cells for cardiac repair: problems and possibilities. - PubMed - NCBI.” [Online]. Available: http://www.ncbi.nlm.nih.gov/pubmed/24180543. [Accessed: 15-Oct-2015].

[68] R. Bolli, A. R. Chugh, D. D’Amario, J. H. Loughran, M. F. Stoddard, S. Ikram, G. M. Beache, S. G. Wagner, A. Leri, T. Hosoda, J. B. Elmore, P. Goihberg, D. Cappetta, N. K. Solankhi, I. Fahsah, D. G. Rokosh, M. S. Slaughter, J. Kajstura, and P. Anversa, “Effect of Cardiac Stem Cells in Patients with Ischemic Cardiomyopathy: Initial Results of the SCIPIO Trial,” *Lancet*, vol. 378, no. 9806, pp. 1847–1857, Nov. 2011.

[69] M. E. Davis, P. C. H. Hsieh, A. J. Grodzinsky, and R. T. Lee, “Custom design of the cardiac microenvironment with biomaterials,” *Circ. Res.*, vol. 97, no. 1, pp. 8–15, Jul. 2005.

[70] A. E. Capito, S. S. Tholpady, H. Agrawal, D. B. Drake, and A. J. Katz, “Evaluation of host tissue integration, revascularization, and cellular infiltration within various dermal substrates,” *Ann. Plast. Surg.*, vol. 68, no. 5, pp. 495–500, May 2012.

[71] S. Goldman and T. E. Raya, “Rat infarct model of myocardial infarction and heart failure,” *J. Card. Fail.*, vol. 1, no. 2, pp. 169–177, Mar. 1995.

[72] R. Klocke, W. Tian, M. T. Kuhlmann, and S. Nikol, “Surgical animal models of heart failure related to coronary heart disease,” *Cardiovasc. Res.*, vol. 74, no. 1, pp. 29–38, Apr. 2007.

[73] J. Ye, L. Yang, R. Sethi, J. Copps, B. Ramjiawan, R. Summers, and R. Deslauriers, “A new technique of coronary artery ligation: Experimental myocardial infarction in rats in vivo with reduced mortality,” *Mol. Cell. Biochem.*, vol. 176, no. 1–2, pp. 227–233, Nov. 1997.

[74] L. A. M. Zornoff, S. A. R. Paiva, M. F. Minicucci, and J. Spadaro, “Experimental myocardium infarction in rats: analysis of the model,” *Arq. Bras. Cardiol.*, vol. 93, no. 4, pp. 434–440, Oct. 2009.

[75] R. Gundamaraju, R. C. Vemuri, R. K. Singla, R. Manikam, A. R. Rao, and S. D. Sekaran, “Strophanthus hispidus attenuates the Ischemia-Reperfusion induced myocardial Infarction and reduces mean arterial pressure in renal artery occlusion,” *Pharmacogn. Mag.*, vol. 10, no. Suppl 3, pp. S557–562, Aug. 2014.

[76] Z. Liu, G. A. Kastis, G. D. Stevenson, H. H. Barrett, L. R. Furenlid, M. A. Kupinski, D. D. Patton, and D. W. Wilson, “Quantitative Analysis of Acute Myocardial Infarct in Rat Hearts with Ischemia-Reperfusion Using a High-

Resolution Stationary SPECT System," *J. Nucl. Med.*, vol. 43, no. 7, pp. 933–939, Jul. 2002.

[77] F. Nijland, O. Kamp, P. M. J. Verhorst, W. G. de Voogt, and C. A. Visser, "Early prediction of improvement in ejection fraction after acute myocardial infarction using low dose dobutamine echocardiography," *Heart*, vol. 88, no. 6, pp. 592–596, Dec. 2002.

[78] T. Yamaguchi, Y. Izumi, Y. Nakamura, T. Yamazaki, M. Shiota, S. Sano, M. Tanaka, M. Osada-Oka, K. Shimada, K. Miura, M. Yoshiyama, and H. Iwao, "Repeated remote ischemic conditioning attenuates left ventricular remodeling via exosome-mediated intercellular communication on chronic heart failure after myocardial infarction," *Int. J. Cardiol.*, vol. 178, pp. 239–246, Jan. 2015.

[79] D. Lloyd-Jones, R. Adams, M. Carnethon, G. De Simone, T. B. Ferguson, K. Flegal, E. Ford, K. Furie, A. Go, K. Greenlund, N. Haase, S. Hailpern, M. Ho, V. Howard, B. Kissela, S. Kittner, D. Lackland, L. Lisabeth, A. Marelli, M. McDermott, J. Meigs, D. Mozaffarian, G. Nichol, C. O'Donnell, V. Roger, W. Rosamond, R. Sacco, P. Sorlie, R. Stafford, J. Steinberger, T. Thom, S. Wasserthiel-Smoller, N. Wong, J. Wylie-Rosett, Y. Hong, and American Heart Association Statistics Committee and Stroke Statistics Subcommittee, "Heart disease and stroke statistics--2009 update: a report from the American Heart Association Statistics Committee and Stroke Statistics Subcommittee," *Circulation*, vol. 119, no. 3, pp. 480–486, Jan. 2009.

[80] R. Van Kerckhoven, R. van Veghel, P. R. Saxena, and R. G. Schoemaker, "Pharmacological therapy can increase capillary density in post-infarction remodeled rat hearts," *Cardiovasc. Res.*, vol. 61, no. 3, pp. 620–629, Feb. 2004.

[81] E. Pueyo, L. Sornmo, and P. Laguna, "QRS Slopes for Detection and Characterization of Myocardial Ischemia," *IEEE Trans. Biomed. Eng.*, vol. 55, no. 2, pp. 468–477, Feb. 2008.

[82] X. Copie, K. Hnatkova, A. Staunton, L. Fei, A. J. Camm, and M. Malik, "Predictive power of increased heart rate versus depressed left ventricular ejection fraction and heart rate variability for risk stratification after myocardial infarction: Results of a two-year follow-up study," *J. Am. Coll. Cardiol.*, vol. 27, no. 2, pp. 270–276, Feb. 1996.

[83] J. V. Monmeneu, F. J. Chorro, V. Bodí, J. Sanchis, A. Llácer, R. García-Civera, R. Ruiz, R. Sanjuán, M. Burguera, and V. López-Merino, "Relationships between heart rate variability, functional capacity, and left ventricular function following myocardial infarction: an evaluation after one week and six months," *Clin. Cardiol.*, vol. 24, no. 4, pp. 313–320, Apr. 2001.

[84] J. J. H. Chong, X. Yang, C. W. Don, E. Minami, Y.-W. Liu, J. J. Weyers, W. M. Mahoney, B. Van Biber, S. M. Cook, N. J. Palpant, J. A. Gantz, J. A. Fugate, V. Muskheli, G. M. Gough, K. W. Vogel, C. A. Astley, C. E. Hotchkiss, A. Baldessari, L. Pabon, H. Reinecke, E. A. Gill, V. Nelson, H.-P. Kiem, M. A. Laflamme, and C. E. Murry, "Human embryonic-stem-cell-derived cardiomyocytes regenerate non-human primate hearts," *Nature*, vol. 510, no. 7504, pp. 273–277, Jun. 2014.

VITA

Frency Varghese

EDUCATION:

PhD - Biomedical Engineering, **GPA 3.87/4.0**, Old Dominion University, VA, 2015

M.S - Bioengineering, **GPA 3.4/4.0**, Syracuse University, Syracuse, NY, December 2009

B.S - Biomedical Instrumentation, **First Class**, University of Mumbai, India, May 2004

B.S – Physics, Mathematics, **First Class**, University of Mumbai, India, May 2000

AWARDS:

ODU Alumni Outstanding Scholar Graduate Fellowship recipient 2013 – 2014

Academic merit scholarship from Syracuse University for Masters in Bioengineering

PEER REVIEWED PUBLICATIONS: (selected)

C. W. Zemlin, **F. Varghese**, M. Wellner, and A. M. Pertsov. "Refraction of Scroll-Wave Filaments at the Boundary Between Two Reaction-Diffusion Media", *Physical Review Letters*, 114, 118303, (2015).

F Varghese, Bukhari AB, Malhotra R, and De A, IHC Profiler: An Open Source Plugin for the Quantitative Evaluation and Automated Scoring of Immunohistochemistry Images of Human Tissue Samples. *PLOS ONE*, 9,e96801, (2014).

CONFERENCE ABSTRACTS: (selected)

B. Hargrave, F. Li, **F Varghese**, and C. W. Zemlin, "Platelet gel activated with nanosecond pulsed electric fields promotes recovery from ischemia and restores electrical activity", Heart Rhythm, Denver, 2013.

F. Xie, **F Varghese**, S. Xiao, and C. W. Zemlin, "Ablation of Myocardial Tissue with Nanosecond Pulsed Electric Fields", Heart Rhythm, Denver, 2013.